Formation of iron oxide–apatite deposits

Martin Reich[1,2]✉, *Adam C. Simon*[3], *Fernando Barra*[1,2], *Gisella Palma*[4], *Tong Hou*[5,6] *and Laura D. Bilenker*[7]

Abstract | Renewed economic interest in iron oxide–apatite (IOA) deposits — containing tens to hundreds of millions of tonnes of Fe and substantial amounts of rare earth elements, P, Co and V — has emerged to supply the sustainable energy transition. However, the mechanisms that efficiently concentrate dense iron-rich minerals (for example, in ores up to ~90% magnetite) at the Earth's near-surface are widely debated. In this Review, we discuss synergistic combinations of magmatic and hydrothermal iron-enrichment processes that can explain the available geochemical, petrological and geological IOA data. IOA deposits typically evolve from subduction-related water-rich and chlorine-rich intermediate magmas under a wide temperature range, almost spanning the whole igneous–hydrothermal spectrum (from ~1,000 to 300 °C). Magmatic–hydrothermal fluids could efficiently scavenge Fe from magmas to form large IOA deposits (>100 million tonnes of Fe), whereas crystal fractionation and liquid immiscibility processes might account for more minor Fe mineralization occurrences. Igneous magnetite crystallization, volatile exsolution and highly focused transport of Fe-rich hydrothermal fluids through the crust under extensional tectonic conditions could be key factors enabling concentration of dense magnetite minerals in the less-dense upper crust. Future research should target both fertile and barren mafic–intermediate magmatic suites for distinctive signatures diagnostic of metallogenic fertility, to help unravel the genetic linkage between IOA and iron oxide–copper–gold systems.

Massive magnetite ore
Mineral assemblage composed of ≲90% magnetite [Fe_3O_4], with variable amounts of apatite, actinolite and/or pyroxene.

Apatite
Group of common phosphate minerals [$Ca_5(PO_4)_3$(F, Cl, OH)] including fluorapatite, chlorapatite and hydroxyapatite.

Actinolite
Calcium magnesium iron silicate mineral of the amphibole group [$Ca_2(Mg_{4.5–2.5}Fe_{0.5–2.5})Si_8O_{22}(OH)_2$].

✉*e-mail:* *mreich@ing.uchile.cl*

https://doi.org/10.1038/s43017-022-00335-3

Sustainable metal supply is an important global challenge of the twenty-first century, with demand for major commodities forecast to increase continuously to the year 2100 (REFS.[1,2]). Among the various metals and their unique applications, iron (Fe) is the basic raw material in steel manufacturing and hence has strategic relevance to the development of related industries[3,4]. Iron oxide–apatite (IOA) deposits, commonly referred to as Kiruna-type or magnetite–apatite deposits, can contain several million tonnes of Fe and are a relevant source of Fe for society. These deposits are also attractive targets for exploration and mining because they contain strategic elements such as phosphorus (P), rare earth elements (REEs), vanadium (V) and cobalt (Co). Global demand for these elements is on the rise because they are critical for current and emerging energy technologies — electric vehicles, wind turbines, photovoltaic cells, batteries and efficient lighting — which are crucial for reducing carbon emissions and mitigating anthropogenic climate change[5–7].

Although IOA deposits have been mined for centuries, they have remained relatively little studied, and it was only in the 2010s that their investigation saw a resurgence. Key to this renewed interest is their economic importance and unique yet varied geological characteristics, which have stimulated controversy about their origin. IOA deposits comprise massive magnetite ore bodies with variable amounts of apatite, actinolite and/or pyroxene (BOX 1). Magnetite is denser (5.15 g cm^{-3}) than the upper crust (~2.7 g cm^{-3}), and therefore it is expected to settle to the bottom of deep magma reservoirs. However, field, textural and chemical evidence indicates that magnetite ore bodies can be emplaced at shallow crustal levels and even at the Earth's surface. For example, the latter is the case for the El Laco deposit in the Central Andes, where outcropping magnetite ore bodies have remarkably similar features to basaltic lava flows[8,9], with degassing and pyroclastic-like structures[10–14]. However, more commonly magnetite mineralization occurs in IOA deposits, forming massive tabular magnetite, lenses, veins, stockworks, breccias, and stratabound or pegmatite-like bodies[15–17] (BOX 1), which are evidence of subvolcanic to deep emplacement[18–21].

These opposing characteristics from different deposits have fuelled debate about whether IOA deposits form from magmas or hydrothermal fluids, renewing a long-standing controversy[15,17,22,23]. This debate has

Key points

- Iron oxide–apatite deposits can form from purely igneous (~1,000–800 °C), through late magmatic or magmatic–hydrothermal (~800–600 °C), to purely hydrothermal (<600 °C) conditions. Cooling trends are identified at deposit to mineral grain scales.
- IOA mineralization is fundamentally controlled by temperature, but relative depth of formation and structural level of emplacement are also relevant factors.
- The source of Fe and other minor metals (for example, Cu and Co) is predominantly linked to intermediate magmas and magmatically derived aqueous fluids, but in some cases there may be a minor contribution from low-temperature, non-magmatic hydrothermal fluids.
- Mechanisms of Fe enrichment are diverse and include a combination of magmatic and hydrothermal processes operating in upper crustal silicate magma reservoirs. Although the relative contributions of each mechanism are still contended, we suggest that magmatic–hydrothermal fluids can efficiently scavenge Fe from magmas to form the largest IOA deposits, whereas crystal fractionation and liquid immiscibility processes might account for smaller Fe mineralization occurrences.
- Tectonic stress changes are key to the formation of large IOA deposits. Fault tapping of silicate magma reservoirs allows for rapid ascent of Fe-rich magmatic–hydrothermal fluids, decompression, and magnetite precipitation upon cooling.

Pyroxene
Most important group of rock-forming ferromagnesian silicates, which includes the clinopyroxene diopside [$CaMgSi_2O_6$].

Stockworks
Structurally controlled or randomly oriented sets of veins that form a three-dimensional network.

Stratabound
An ore body confined to a single stratigraphic level or unit.

Pegmatite
Intrusive igneous rock occurring as dykes, veins or lenses, and consisting almost entirely of centimetre-sized crystals.

Silicate liquid immiscibility
Process leading to formation of mixtures of distinct iron-rich and silica-rich melts from one parental silicate magma.

endured because the two classical contrasting hypotheses — silicate liquid immiscibility and separation of an Fe–P-rich melt[24–28] versus metasomatic replacement of host rocks by Fe-rich fluids[29–33] from magmatic and/or non-magmatic sources[34–38] — are usually considered as mutually exclusive and have failed to provide a general model that encompasses all geological observations and geochemical data from IOA deposits around the world.

In this Review, we present an overview of IOA deposits, their main characteristics, global distribution, and analytical and experimental data to better understand IOA formation conditions and iron-enrichment processes. A particular emphasis is given to multiproxy geochemical data of magnetite, the main ore mineral. We explain how trace elements can help to constrain the geological environment of magnetite formation, and how stable isotopes can fingerprint the source of Fe. In addition, we review experimental results exploring the thermodynamic conditions at which IOA systems might form in nature, and the most plausible Fe concentration mechanisms in the formation of large deposits. This information provides a framework to better understand the metallogenesis of IOA deposits worldwide, which involves processes spanning the entire igneous–hydrothermal range. Finally, we integrate analytical and experimental data into our preferred general conceptual model of IOA formation in arc settings, which, as with every model, should be tested with future research to further improve understanding of IOA formation and exploration strategies, and to find new resources.

Author addresses

[1]Department of Geology and Andean Geothermal Center of Excellence (CEGA), FCFM, Universidad de Chile, Santiago, Chile.
[2]Millennium Nucleus for Metal Tracing Along Subduction, FCFM, Universidad de Chile, Santiago, Chile.
[3]Department of Earth and Environmental Sciences, University of Michigan, Ann Arbor, MI, USA.
[4]Escuela de Geología, Universidad Mayor, Santiago, Chile.
[5]State Key Laboratory of Geological Processes and Mineral Resources, China University of Geosciences, Beijing, China.
[6]Institut für Mineralogie, Leibniz Universtät Hannover, Hannover, Germany.
[7]Department of Geosciences, College of Sciences and Mathematics, Auburn University, Auburn, AL, USA.

Global distribution in space and time

IOA deposits are globally distributed and formed throughout geological time[39–43] (FIG. 1). They are preferentially found in volcano-plutonic provinces from the Palaeoproterozoic to the Pleistocene, and they are commonly related to extensional tectonic regimes, often within a subduction setting[44–48], although they also occur in other geological environments, for example associated with A-type granitoids[39,42]. Metal endowment of IOA deposits can reach hundreds to thousands of million tonnes of Fe ore, which occur as high-grade (>40–50% total Fe) magnetite ore bodies exhibiting distinct geological and mineralogical characteristics (BOX 1), some of which are also common to iron oxide–copper–gold (IOCG) deposits[49–54]. IOA deposits should not be confused with nelsonites, which are commonly associated with anorthositic complexes and layered mafic intrusions[55–58], and differ in origin from typical IOA deposits[44,54,59,60] (BOX 1).

The most prominent IOA deposits are those found near Kiruna in northern Sweden, the type locality of these magnetite–apatite deposits (FIG. 1). Other world-class districts occur in central Sweden, Missouri (USA), Iran and most notably Chile. Similar deposits are found in China[61], New York (USA)[62], Mexico[63] and Peru[64], among several occurrences around the globe including Canada[65,66], Turkey[67], Sri Lanka[68] and Korea[69]. Besides the main IOA districts in Sweden, the United States, Iran and Chile, which are described in more detail below, the Middle–Lower Yangtze River Metallogenic Belt in China contains several IOA deposits within the Cretaceous Ningwu and Luzong terrigenous volcanic basins[61,70,71]. These deposits contain magnetite and apatite in brecciated, massive, and vein ore bodies that are spatially and temporally associated with dioritic subvolcanic intrusions, probably related to back-arc extensional tectonics[61].

The world's largest and most famous IOA deposit is the Palaeoproterozoic (~1.90–1.86 Ga) Kiirunavaara deposit in the Kiruna Mining District, Norrbotten region[72,73]. It contains more than 2,000 million tonnes (Mt) of high-grade ore (50–70% Fe), dominated by magnetite, minor apatite and monazite, and is thought to have formed in an arc-related extensional setting[74–78]. The IOA deposits in the Grängesberg Mining District in the Bergslagen region of central Sweden are traditionally grouped together with those of the Kiruna region. The Grängesberg deposit was also formed during the Palaeoproterozoic (~1.9–1.88 Ga), and contains ~421 Mt ore averaging 60% Fe, with dominant magnetite, fluorapatite, monazite, xenotime and REE-silicates. A subduction- or back-arc-related tectonic setting has been proposed for its formation[18,79,80].

The early Mesoproterozoic St Francois Mountains terrane in southeast Missouri, USA, contains prominent IOA mineralization, formed between ~1.50 and 1.44 Ga (REFS.[19,81–83]). The IOA deposits[84–88] are associated

Box 1 | **Main characteristics of iron oxide–apatite deposits**

Iron oxide–apatite (IOA) deposits, also known as Kiruna-type or magnetite–apatite deposits, are characterized by distinct geological and mineralogical features.

- They represent the Cu-poor endmember of iron oxide–copper–gold (IOCG) deposit types, a geologically diverse group of deposits containing >10% low-Ti Fe oxides and elevated contents of Cu, Au, rare earth elements, P, U, Ag, Co and V[39–43]. IOA ore bodies are often structurally controlled and are dominantly associated with volcanic and intrusive rocks of intermediate composition and calc-alkaline affinity. Sodic and Ca–Na hydrothermal alteration and/or metasomatism are widespread[44–47].
- Strictly, IOA deposits are not IOCGs but can share certain commonalities with them, including the abundance of early-stage magnetite, actinolite and apatite in many IOCG deposits, and the presence of late-stage pyrite, chalcopyrite and gold in some IOA deposits[41,42,47–49]. These similarities suggest a genetic relationship between IOA and IOCG mineralization styles, including the possibility that they represent a continuum, although mineralization is not necessarily coeval[50–54].
- IOA deposits should not be confused with nelsonites, which are named for the type locality Nelson, Virginia, USA. Nelsonites are dominated by ilmenite with 30–50% modal apatite, and they do not contain magnetite. Strictly, nelsonites are composed of ilmenite, although the term is often loosely applied to deposits that contain Ti-rich magnetite, commonly associated with anorthositic complexes (90–100% modal plagioclase) and the upper parts of layered mafic intrusions[23,55–58].
- Magnetite is the main constituent of IOA deposits, with variable amounts (1–50% modal) of apatite, actinolite and/or pyroxene. Other gangue minerals that might be present include pyrite, biotite, scapolite, chlorite, titanite, calcite and late quartz. Pyrite can occur as disseminated grains, massive sulfide veins and veinlets associated with late magnetite and actinolite; it is the dominant sulfide and can contain up to wt% levels of cobalt[49]. Martite (haematite replacing magnetite) can be common.
- The size of IOA deposits vary from those endowed with many hundreds of million tonnes of Fe ore to smaller deposits containing a few tens of million tonnes of Fe ore. They exhibit varied styles of mineralization, which include massive tabular bodies, breccias, veins, veinlets and stockworks, as well as disseminations and concordant replacements in permeable volcanic and volcano-sedimentary host rocks[17,41,42,44,46].
- The field photos illustrate three contrasting mineralization styles in the Chilean Andes, one of the world's premier IOA provinces (panels **a**–**c** of the figure). The surface ore bodies at the Plio-Pleistocene El Laco deposit[8] in the Chilean Altiplano form lava-like massive magnetite deposits (≲90% magnetite), and are representative of the subvolcanic and/or aerial type[20] (panel **a**). At Carmen[59], in the Cretaceous Chilean Iron Belt, magnetite forms irregular ore bodies, breccias and veins, with large apatite crystals (up to 50 cm), which are typical of the pegmatitic type[20] (panel **b**). Deeply emplaced, intrusive-like systems such as the Los Colorados deposit[60] in the Chilean Iron Belt are often characterized by kilometre-scale tabular massive magnetite bodies or dykes, with stockwork and breccias[20] (panel **c**).

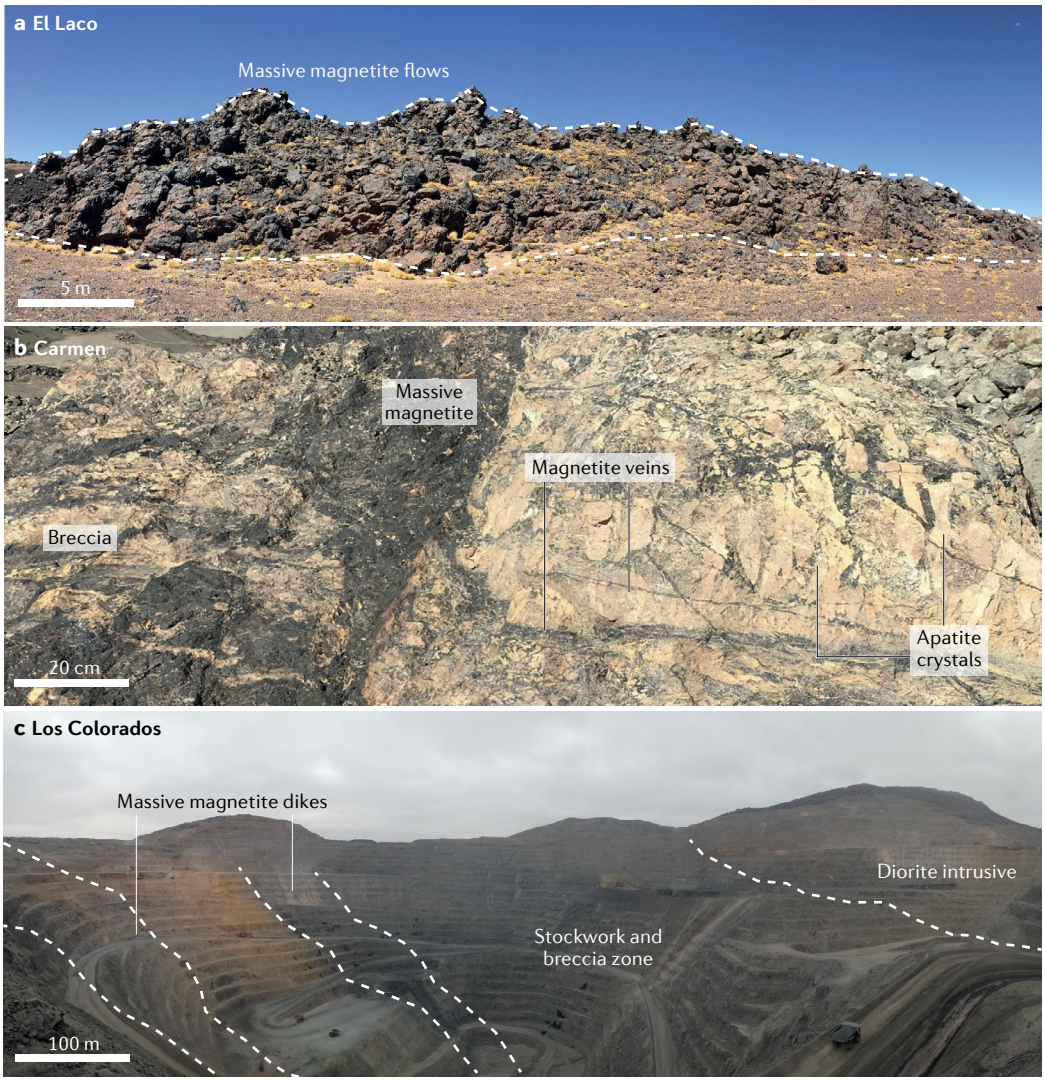

with bimodal volcanic sequences, some of which have arc affinities, suggesting construction on juvenile continental crust in an arc setting that transitioned to an extensional regime[19]. Pea Ridge is the most important IOA deposit in the district, with ~160 Mt of massive magnetite ore (>50–60% Fe) crosscut by REE-bearing breccia pipes[19,89–92].

The Palaeozoic Bafq Mining District of central Iran contains ~2,000 Mt of Fe ore reserves distributed among dozens of high-grade (53–65% Fe) deposits; for example,

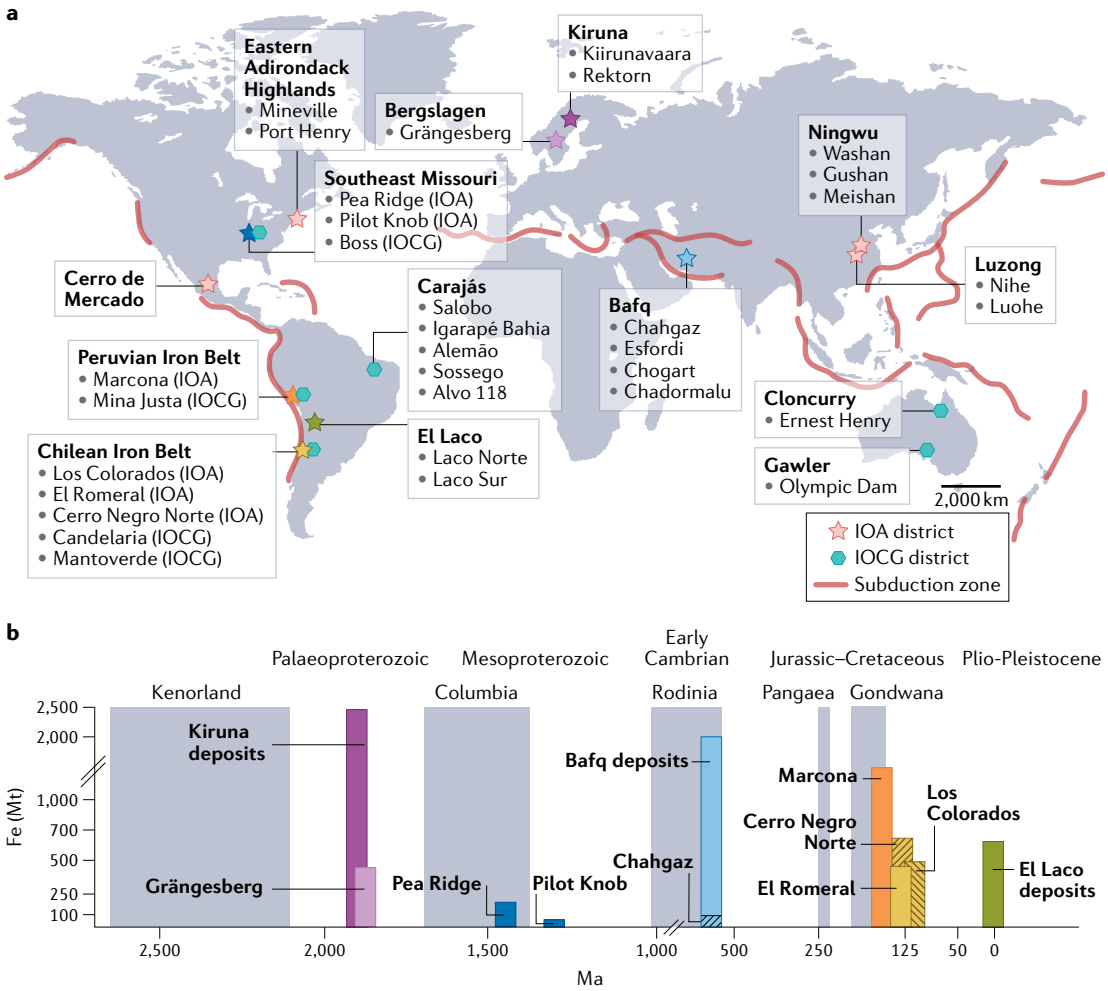

Fig. 1 | **Spatial and temporal distribution of main iron oxide–apatite districts.** Iron oxide–apatite (IOA) deposits are distributed worldwide and have formed repeatedly over the history of the Earth, from the Palaeoproterozoic to the Plio-Pleistocene. **a** | IOA deposits are typically related to subduction-related extensional tectonic settings. IOA deposits (stars) can display spatial and temporal associations with iron oxide–copper–gold (IOCG) systems (hexagons), a feature most notably observed in the Andean province. Key deposits and districts are highlighted in bold. **b** | Temporal distribution of large (>100 Mt) IOA deposits, including their relation to the supercontinent cycle (grey blocks). Ma, million years ago. The bar colours match the symbols in **a**. The formation of key IOA districts is broadly coincident with the break-up of the supercontinents Kenorland, Columbia, Rodinia and Gondwana[42]. Panel **b** was adapted with permission from REF.[42], Society of Economic Geologists; using data from REFS.[14,19,45,46,64,74,79,84,93,98,100,108,123,147,164].

Chadormalu, Choghart, Esfordi and Chahgaz[16,93,94]. Magnetite is the most common ore mineral — often oxidized to haematite — with abundant apatite and actinolite[95–98]. The IOA deposits of the Bafq region are coeval with their Late Neoproterozoic to Early Cambrian (~547–525 Ma) andesitic and rhyolitic host rocks, which formed in a continental arc environment[99,100].

Large IOA deposits of Mesozoic to Cenozoic age are located in the Andean Cordillera of western South America. The Marcona deposit in Peru contains ~1,900 Mt of high-grade ore (55% Fe) and was formed associated with an andesitic, shallow-marine arc during the Late Jurassic (162–156 Ma)[64,101]. The largest deposits in the Andean province are located in the Cretaceous Chilean Iron Belt[17,46,47,102], with pre-eminent deposits such as Los Colorados (491 Mt, 36.5 wt% Fe)[60,103–105], El Romeral (451 Mt, 28.3% Fe)[45,106,107] and Cerro Negro Norte (657.3 Mt, 29.7% Fe)[108]. In the Chilean Iron Belt, IOA deposits consist of massive tabular magnetite ore bodies with variable amounts of actinolite and apatite, and were formed during the Early Cretaceous (~130–110 Ma)[44,47,109,110] when the South American subduction zone transitioned from an arc-normal extensional to an oblique transtensional regime[111].

The youngest and most iconic member of the IOA deposits is the Plio-Pleistocene El Laco deposit in the Altiplano of northern Chile[8,14,17] (FIG. 1). El Laco is hosted by volcanic products that range from 5.3 to 1.6 Ma (REFS.[112–116]). The ore bodies are largely composed of magnetite with minor diopside, apatite, REE-rich and Fe phosphates, with a haematite–goethite supergene alteration[17,37,117–119]. Resources have been estimated at 733.9 Mt with an average grade of 49.2% Fe[14].

The global occurrence and age distribution of IOA deposits indicate that they formed repeatedly throughout Earth's history, commonly related (but not limited)

Metasomatic replacement
Fluid-driven replacement process of one mineral or a mineral assemblage by another of different composition, while the rock remains solid.

Arc settings
Tectonic environments where one oceanic plate subducts beneath another oceanic plate, or under a continental plate.

to extensional tectonic regimes in subduction settings, and predominantly linked to calc-alkaline volcanic and intrusive rocks of intermediate composition.

Formation conditions and source

Microanalytical investigations[14,20,71,120,121] and stable isotope analyses[60,79,118,122,123] of magnetite have proven key to obtain reliable petrogenetic information on IOA systems. Magnetite forms under a wide range of conditions, from purely igneous to magmatic–hydrothermal, metamorphic or sedimentary and basinal settings. Physico-chemical parameters, such as temperature, pressure and oxygen fugacity, typical of each formation environment, lead to distinctive trace-element signatures in magnetite. In addition, iron and oxygen (the two essential components of magnetite) and their respective isotope compositions provide robust constraints among different sources for magmas and hydrothermal fluids. Therefore, present knowledge about the formation of IOA deposits is largely based on trace-element geochemistry and the stable Fe–O isotope composition of magnetite, which is the modally dominant mineral in all IOA deposits.

Igneous to hydrothermal transition. The great diversity of trace elements that can be incorporated into magnetite, for example, Ti, V, Mg, Al, Mn, Co, Ni, Zn, Cr and Ga, has made this mineral valuable for study because of its capacity to record chemical gradients reflective of melt-fluid composition and elemental partitioning conditions[124–127]. Therefore, the trace-element geochemistry of magnetite and its genetic interpretation have been extensively explored to differentiate among various types of Fe mineralization[128–131]. This approach has been applied comprehensively in the Cretaceous Iron Belt and El Laco deposit in Chile (FIG. 1). The low degrees of deformation, metamorphism and alteration, and high level of preservation make this region particularly useful for genetic interpretations. Thus, trace-element data of magnetite from Chilean deposits can be used as a geochemical proxy for other IOA districts[20,21,60,103,132].

Among the many proposed trace-element diagrams[20,103,120,125,128], the [Ti + V] versus [Al + Mn] plot[130] reveals geochemical trends for magnetite[20] (FIG. 2a; with corresponding data compilation provided in Supplementary Data). Magnetite data from IOA deposits in the Chilean Iron Belt and El Laco spread over several deposit-type fields, from purely igneous affinity defined by high [Ti + V] and [Al + Mn] contents (magmatic Fe–Ti, V deposits associated with anorthosites), through high-temperature, magmatic–hydrothermal compositions defined by intermediate contents of [Ti + V] and [Al + Mn] (porphyry, skarn and Kiruna deposits fields), to lower-temperature hydrothermal affinities characterized by depleted concentrations of the aforementioned element pairs (Kiruna and IOCG fields) (FIG. 2a).

Combined chemical mapping and spot analysis of magnetite grains have provided more details on the ore-forming conditions[20,46,60,103] (FIG. 2b). At the Los Colorados IOA deposit in the Chilean Iron Belt, electron microprobe analysis and laser ablation inductively coupled plasma mass spectrometry (LA-ICP-MS) data show that high Ti and Mg contents, among other elements, are ubiquitously concentrated in the cores of magnetite grains (Mgt-1) (FIG. 2b), similarly to high-temperature magnetite crystallized from a silicate magma[46,60,103,130]. Qualitatively, the systematic decrease in Ti and Mg from core to rim (FIG. 2b) is distinctive of magnetite that was precipitated from magmatic–hydrothermal fluids of high to intermediate temperature (Mgt-2 and Mgt-3)[46,60,103,130]. The magnetite crystallization temperature can be qualitatively estimated at the grain scale using the Mg and Fe concentration ($T_{Mg\text{-}mag}$)[133]. Temperatures for magnetite in the Los Colorados deposit configure a cooling trend in the [Ti + V] vs [Al + Mn] plot, with magnetite cores displaying the highest temperature conditions ($T_{Mgt\text{-}1} \approx 800–630\,°C$), followed by mantles recording intermediate temperatures ($T_{Mgt\text{-}2} \approx 730–550\,°C$) and rims showing the lowest temperatures ($T_{Mgt\text{-}3} \approx 650–530\,°C$) (FIG. 2a). Although the reader should note that the application of $T_{Mg\text{-}mag}$ to hydrothermal magnetite is limited by the geothermometer calibration and by the potential presence of Mg–Fe-bearing nanoscale inclusions[132–135], the $T_{Mg\text{-}mag}$ geothermometer consistently yields igneous temperatures in primary magnetite and subsolidus temperatures (<600 °C) in hydrothermal magnetite[133]. Thus, the $T_{Mg\text{-}mag}$ has a potential application in igneous or hydrothermally altered rocks where conventional thermometers are not appropriate[133]. As such, $T_{Mg\text{-}mag}$ data are discussed here as a proxy for temperature in IOA systems, and compared to temperature estimations based on fluid inclusion and stable isotope thermometry, among other methods.

It should be noted that despite concerns about the use of trace-element data to estimate conditions of magnetite formation, and potential effects of post-crystallization processes that might modify the original composition[134–138], magnetite data in IOA systems usually form a distinctive cooling trend from igneous to hydrothermal signatures (FIG. 2a,b). This trend, exemplified here for magnetite from Chilean deposits, is documented in many IOA districts worldwide, for example, in deposits from Missouri, USA[88], in Luzong, eastern China[139], in Kiruna, northern Sweden[140], and in Bafq, Iran[98,141]. Similar compositional variations are also observed in coeval apatite, where early formed, igneous-like (F-rich) apatite compositions transition or are altered to late, Cl-rich varieties that are typical of hydrothermal environments[105,110,119].

Temperature and relative depth of formation. The documented transition from igneous to magmatic–hydrothermal conditions is a first-order feature of IOA systems (FIG. 2a,b), suggesting that temperature is a critical parameter controlling mineralization. Precise determination of mineralization temperatures in IOA deposits has been hindered by the scarce presence of quartz amenable to fluid inclusion microthermometry, particularly in the high-temperature Na–Ca alteration assemblages. Therefore, reported temperature estimations are based on data obtained from fluid inclusions[92,142–144] in other phases including apatite, actinolite, pyroxene, anhydrite and calcite[115,145–148], mineral inclusions in apatite and magnetite[80,107,108,149], magnetite–ilmenite pairs[116,150], Fe content in actinolite[51,107,122,151], and oxygen

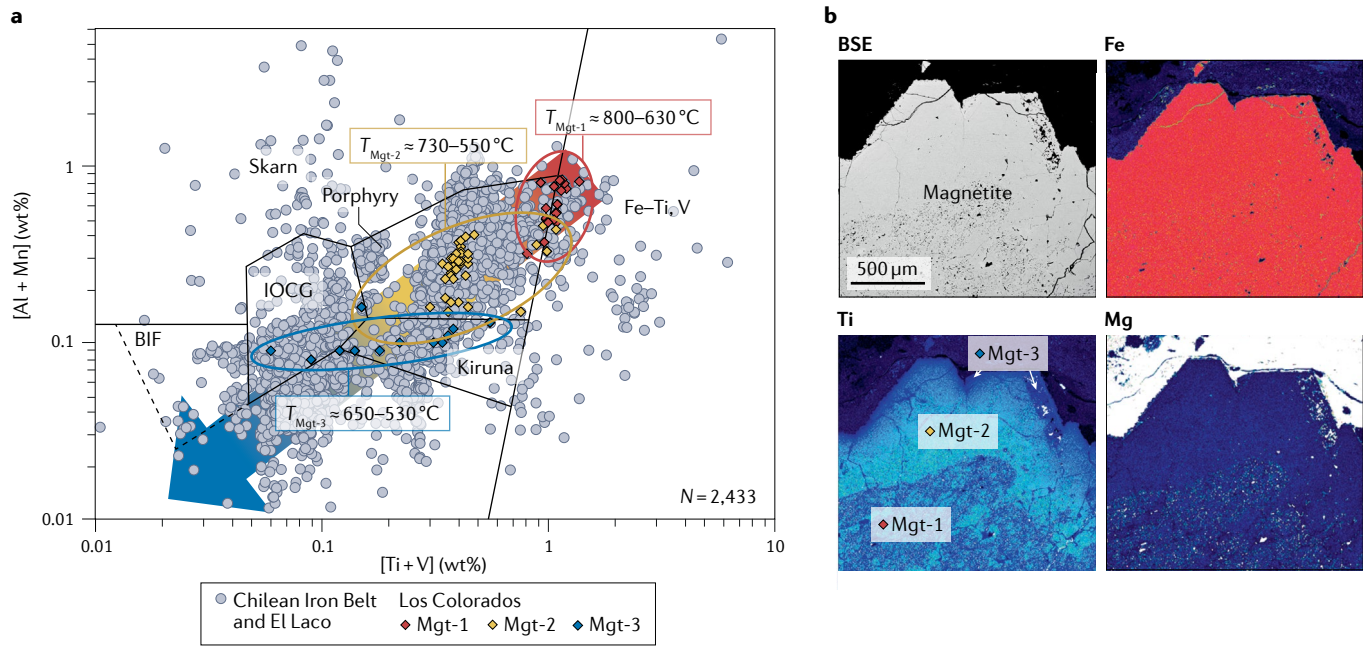
a
[Al + Mn] (wt%)
[Ti + V] (wt%)
Skarn
Porphyry
IOCG
BIF
Kiruna
Fe–Ti–V
T_{Mgt-1} ≈ 800–630 °C
T_{Mgt-2} ≈ 730–550 °C
T_{Mgt-3} ≈ 650–530 °C
N = 2,433
Chilean Iron Belt and El Laco
Los Colorados
Mgt-1
Mgt-2
Mgt-3
b
BSE
Fe
Ti
Mg
Magnetite
500 µm
Mgt-3
Mgt-2
Mgt-1

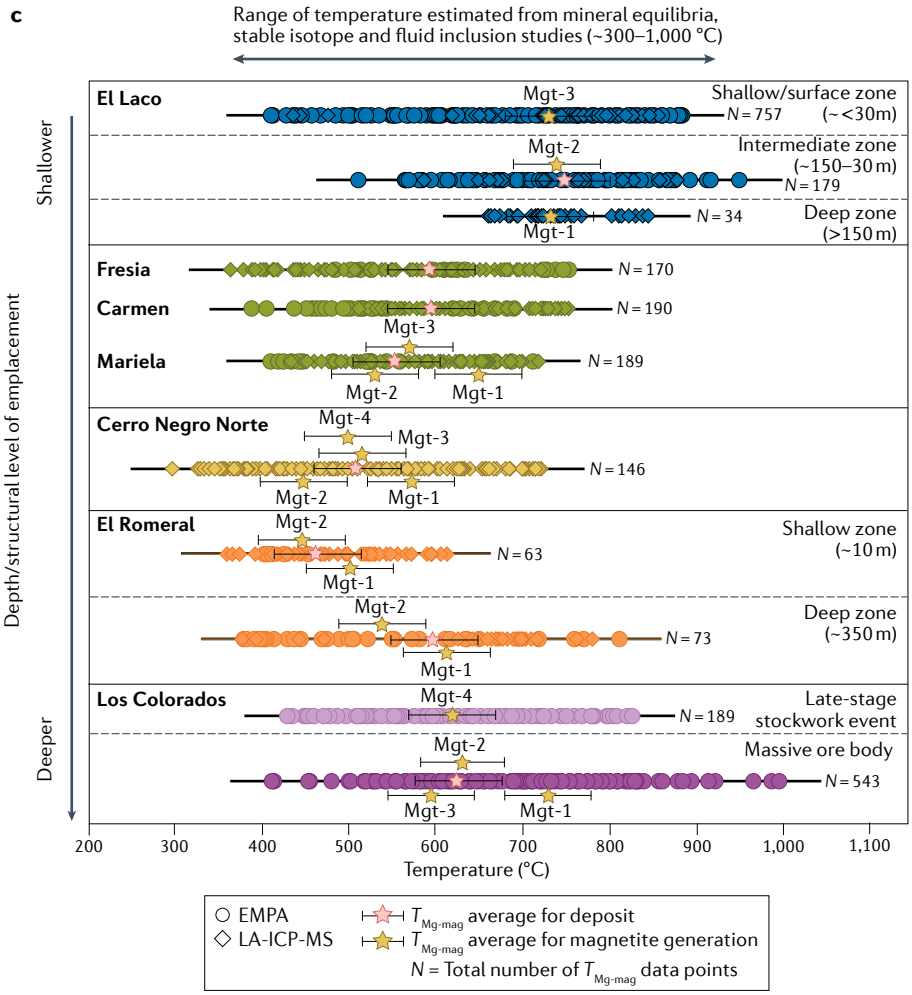
c
Range of temperature estimated from mineral equilibria, stable isotope and fluid inclusion studies (~300–1,000 °C)
Depth/structural level of emplacement
Shallower
Deeper
El Laco
Shallow/surface zone (~<30m)
N = 757
Intermediate zone (~150–30 m)
N = 179
Deep zone (>150 m)
N = 34
Fresia
N = 170
Carmen
N = 190
Mariela
N = 189
Cerro Negro Norte
N = 146
El Romeral
Shallow zone (~10 m)
N = 63
Deep zone (~350 m)
N = 73
Los Colorados
Late-stage stockwork event
N = 189
Massive ore body
N = 543
Mgt-1
Mgt-2
Mgt-3
Mgt-4
200
300
400
500
600
700
800
900
1,000
1,100
Temperature (°C)
EMPA
LA-ICP-MS
T_{Mg-mag} average for deposit
T_{Mg-mag} average for magnetite generation
N = Total number of T_{Mg-mag} data points

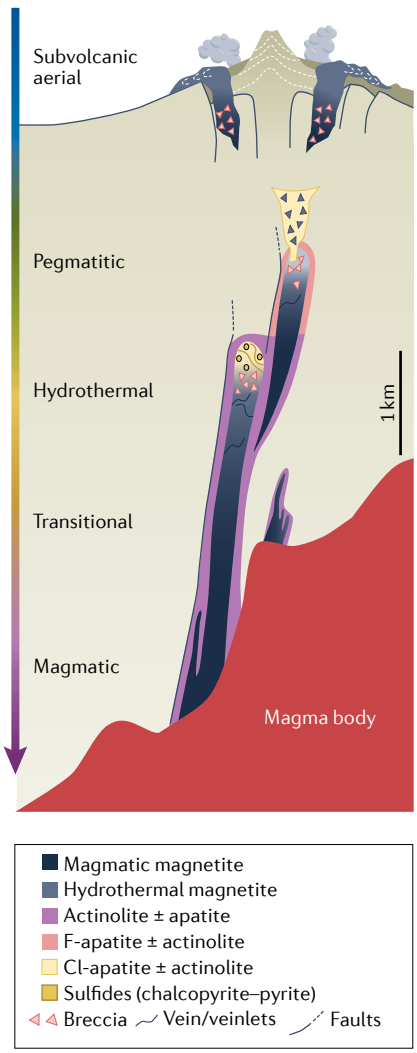
d
Subvolcanic aerial
Pegmatitic
Hydrothermal
Transitional
Magmatic
1 km
Magma body
Magmatic magnetite
Hydrothermal magnetite
Actinolite ± apatite
F-apatite ± actinolite
Cl-apatite ± actinolite
Sulfides (chalcopyrite–pyrite)
Breccia
Vein/veinlets
Faults

◀ Fig. 2 | **Temperature and depth conditions of magnetite formation.** Geochemical trends of magnetite point to a magmatic–hydrothermal origin for iron oxide–apatite (IOA) deposits. **a** | The [Ti + V] versus [Al + Mn] diagram[130] shows a compilation of electron microprobe analyses (EMPA) of magnetite from the Chilean Iron Belt and El Laco deposit (grey points; data from REFS.[14,20,60,103,107,108,132]; and provided in the Supplementary Data). Magnetite data for the Los Colorados deposit (coloured diamonds) configure a well-defined trend of decreasing [Ti + V] and [Al + Mn] concentrations. Estimated temperatures, obtained for each texturally controlled data point using Mg concentrations in magnetite[133], configure a cooling trend from igneous to magmatic–hydrothermal conditions, represented by the arrow ($T_{Mgt\text{-}1} > T_{Mgt\text{-}2} > T_{Mgt\text{-}3}$). **b** | Compositional variations of magnetite at the mineral grain scale. The upper left image shows a back-scattered electron (BSE) image of a representative magnetite grain from the Los Colorados deposit. The other three panels show Fe, Ti and Mg wavelength-dispersive spectrometry (WDS) X-ray maps of the same grain. WDS maps show that magnetite exhibits a distinct zonation in composition and temperature, with higher contents of Ti and Mg in the core (Mgt-1), which decrease towards the mantle (Mgt-2) and rim (Mgt-3) (see panel **a**). **c** | Thermal evolution and relative depth of emplacement of IOA deposits, using estimated temperatures from the Mg-in-magnetite data[21,133] for deposits in the Chilean Iron Belt and El Laco. For each deposit, coloured data diamonds show individual temperatures while the stars represent the average temperature for each deposit (pink stars) and the different textural types, from the earliest- to the latest-formed (yellow stars, from Mgt-1, -2, -3, -4). The arrow above the figure shows the temperature range of magnetite formation determined from mineral equilibria, stable isotope data and fluid inclusion thermometry (see text for references). $T_{Mg\text{-}mag}$ data are ±50 °C. **d** | The cooling trend broadly correlates with the relative depth of ore formation, with intrusive-like deposits (Los Colorados, El Romeral) having magmatic–hydrothermal characteristics and higher temperatures. Deposits formed at shallower levels show progressively lower temperatures and hydrothermal- or pegmatitic-like features (Cerro Negro Norte, Carmen, Fresia, Mariela). The El Laco deposit represents an eruptive (subvolcanic to aerial) endmember. BIF, banded iron formation; IOCG, iron oxide–copper–gold; LA-ICP-MS, laser ablation inductively coupled plasma mass spectrometry. Panels **a** and **b** adapted with permission from REF.[60], Geological Society of America. Panel **c** modified from REF.[21], CC BY 4.0. Panel **d** adapted with permission from REF.[20], Elsevier.

isotope thermometry[122,152–155]. These methods yield temperatures between ~1,000 and 300 °C.

Temperature estimates using trace-element data in magnetite[133] from Chilean IOA deposits overlap those obtained by these other methods, spanning almost the whole igneous–hydrothermal spectrum; for example, from ~1,000 to 300 °C (FIG. 2c). The temperature data consistently record igneous and subsolidus conditions[133] that match those determined by mineral equilibria, stable isotope and fluid inclusion results cited above. Notwithstanding this, more research and experiments are needed to closely examine temperature and other intensive variables in IOA systems, which could have an impact on elemental partitioning in magnetite at the igneous–hydrothermal transition.

When magnetite temperature data are compared among deposits formed at different depths or structural levels within the Chilean Iron Belt and El Laco[21], it is observed that the deeply emplaced, intrusive-type Los Colorados deposit records the highest temperatures, mostly ranging between ~850 and 500 °C, whereas the transitional-type El Romeral deposit is characterized by intermediate temperatures (~780–340 °C), followed by lower temperatures in the hydrothermal-type Cerro Negro Norte deposit (~700–320 °C) (FIG. 2c). The pegmatitic-type deposits of Mariela, Fresia and Carmen yield similarly lower temperatures (~750–360 °C), while the subvolcanic or aerial-type deposit of El Laco shows a broad range of temperature (~900–359 °C) that tails off towards lower temperatures (~400–350 °C) (FIG. 2c). Interestingly, this qualitative trend of decreasing temperature is also observed for magnetite from different depths within individual deposits. For example, estimated temperatures for the El Romeral and El Laco deposits decrease from the deep zone to shallow levels (FIG. 2c).

Estimated temperatures can be coupled with microtextural observations and trace-element data to assess temporality and reconstruct the thermal evolution of magnetite within individual deposits[60]. Notably, temperatures recorded in early magnetite are consistently higher than paragenetically late generations in most deposits, with temperatures configuring a cooling trend from the earliest to the latest magnetite generation (for example, $T_{Mgt\text{-}1} > T_{Mgt\text{-}2} > T_{Mgt\text{-}3}$) (FIG. 2c).

The distinct cooling trend in FIG. 2c broadly corresponds with the relative depth of formation or structural level of emplacement of the ore bodies (FIG. 2d). Depth of emplacement for IOA deposits is estimated at 3–5 km (~100–200 MPa) based on geological observations and mineral zonation[17,19,44], geophysical imaging[156,157], phase equilibria of ore assemblages[45,107,108,151], and depth of crystallization of plutons associated with mineralization[30,111,158]. These estimations indicate that the observed changes in chemical composition and temperature of magnetite are likely to reflect evolving conditions, from purely igneous at depth to hydrothermal at shallow levels[20,21,46].

Consequently, deposits emplaced at considerable depth often display dominantly magmatic–hydrothermal characteristics and high temperatures, whereas deposits formed at shallower depths show progressively lower temperatures and hydrothermal characteristics (FIG. 2d). These apparent differences also depend on the structural architecture, the composition of the host rocks, and the source and flux rate of hydrothermal fluids, among other factors[20,78]. Although the temperature versus relative depth trends are discussed here for deposits in the Andean province, this relation has been described in many other IOA districts worldwide[16,19,78]. For example, in the Missouri district, metal endowments and ore mineral and alteration assemblages vary systematically with depth, with IOA systems emplaced at diverse crustal levels[19]. Similar relations are observed in the Peña Colorada and Arrayanes IOA deposits in Colima, Mexico, where differences in the pervasiveness and abundance of alteration assemblages suggest distinct differences in emplacement depth[159]. In this scheme, El Laco deposit in the Chilean Altiplano would represent an IOA system emplaced at shallow, subaerial levels within a volcanic system[14].

Magmatic source of Fe. Stable isotopes of Fe and O have been critical to fingerprint the source reservoir(s) of the Fe ore and hydrothermal ore fluids and have provided new insights into the formation of IOA deposits[60,79,122,123]. An advantageous approach involves correlating the $^{56}Fe/^{54}Fe$ isotope ratios, expressed as $\delta^{56}Fe$ per mil (‰) values[160], typically determined relative to the IRMM-14 reference material, with the oxygen system ($^{18}O/^{16}O$) represented by $\delta^{18}O$ (‰) values relative to SMOW (standard mean ocean water)[161]. Fe–O isotope correlations have proven robust geochemical tracers for IOA systems

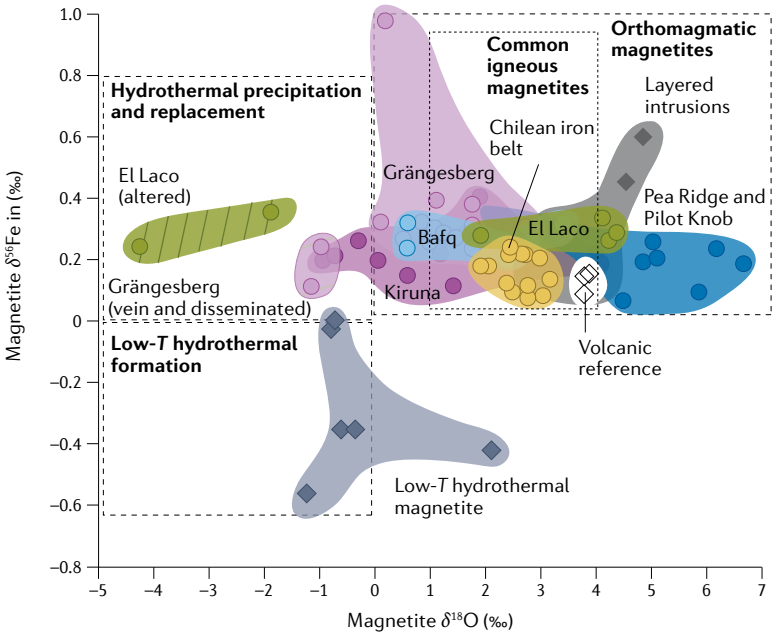

Fig. 3 | **Metal source of IOA deposits.** Fe–O isotope data allow one to fingerprint the source reservoir(s) of the Fe ore. $\delta^{18}O$ versus $\delta^{56}Fe$ values of magnetite from deposits in Kiruna, Grängesberg, Bafq, Missouri, Chilean Iron Belt and El Laco are plotted and contoured as coloured fields that correlate with those in FIG. 1 (data from REF.[123]). Eighty per cent of the Fe–O data lie within the reference boxes of common igneous (short-dashed line) and orthomagmatic magnetite, indicating a predominantly magmatic, high-temperature origin[123]. Only 20% of the Fe–O data overlap with reference boxes of hydrothermal precipitation and replacement and low-temperature hydrothermal formation[123]. $\delta^{18}O$ and $\delta^{56}Fe$ values are relative to SMOW and IRMM-14 standards, respectively. Figure modified from REF.[123], CC BY 4.0.

given the overall chemically resistant nature of magnetite when occurring as massive ore bodies, although supergene alteration can modify the isotopic composition due to oxidation[118,122,123,162].

The $\delta^{18}O$ values of magnetite from IOA deposits in Sweden, Chile, Missouri and Iran range mostly between ~0‰ and +5‰, which are consistent with data for igneous magnetite from plutonic and volcanic reference materials[79,122,123] (FIG. 3). Isotope fractionation calculations indicate that the $\delta^{18}O$ signature of the massive magnetite ore bodies reflect equilibrium either with an intermediate magma ($\delta^{18}O$ between +5.7‰ and +8.7‰) or a magmatically derived high-temperature aqueous fluid ($\delta^{18}O$ between +5.2‰ and +9.6‰), although discriminating between these two possible sources is challenging[79,123]. By contrast, the lighter signatures ($\delta^{18}O < 0$‰) mostly correspond to veins and disseminated magnetite or highly altered or oxidized magnetite[60,79,118,122,123], which are not in equilibrium with magmatic sources but overlap with low-temperature and hydrothermal magnetite reference materials[123]. These variations in isotope signatures are indicative of precipitation from a cooling magmatic–hydrothermal fluid or from externally derived, low-temperature hydrothermal fluids[118,123] (FIG. 3).

Iron isotopes in magnetite show a narrow and consistent range of $\delta^{56}Fe$ values, mostly from about +0.1‰ to +0.5‰[104,122,123] (FIG. 3). As with $\delta^{18}O$ data, the published $\delta^{56}Fe$ values of magnetite from IOA deposits overlap with the magmatic and/or high-temperature field, indicating crystallization from a silicate melt or a magmatic–hydrothermal fluid[60,88,104,118,122,123]. Iron isotope equilibrium calculations for the same magnetite samples where oxygen isotope data are available[110,122,123] yielded $\delta^{56}Fe$ values typical of silicate melts (+0.08‰ to +0.38‰) and magmatic–hydrothermal fluids (−0.13‰ to +0.17‰), and are in agreement with reported $\delta^{56}Fe$ values of intermediate igneous rocks and magmatic waters[123]. Analyses coupling in situ Fe isotope data and trace-element concentrations in magnetite indicate an igneous or magmatic–hydrothermal origin, with grains exhibiting a distinct core-to-rim trend, from higher toward lower $\delta^{56}Fe$ signatures[104]. The narrow range of $\delta^{56}Fe$ data and the absence of negative values typical of hydrothermal magnetite reference materials attest to the robustness of Fe isotopes, whereas O isotopes are more susceptible to post-crystallization alteration or oxidation (FIG. 3).

Global Fe–O isotope correlations allow a systematic evaluation of the magmatic–hydrothermal nature of IOA deposits[123]. Almost 80% of magnetite data from the most relevant IOA districts worldwide show $\delta^{56}Fe$ and $\delta^{18}O$ values that overlap with plutonic and volcanic reference materials, reflecting equilibrium with either an intermediate silicate melt or a high-temperature (>800 °C) magmatic–hydrothermal fluid[123]. By contrast, only ~20% of the magnetite Fe–O data in the studied deposits overlap with reference suites of hydrothermal magnetite and appear in equilibrium with hydrothermal fluids at temperatures ≤400 °C (REF.[123]). These results are in agreement with radiogenic and stable isotope data obtained from apatite, zircon and magnetite related to IOA ore bodies, and from intrusive and host rocks associated with IOA mineralization[44,76,77,90,91]. Collectively, the Sr, Nd, Hf, Pb, Os, Mg and S isotope data fingerprint a magmatic source with a predominant primitive, mantle-like component with variable but limited crustal contribution[108–110,150,163,164].

The available magnetite trace-element and Fe–O isotope data are therefore consistent with a magmatic–hydrothermal origin for IOA deposits, pointing to intermediate magmas and/or magmatically derived high-temperature aqueous fluids as agents of mineralization.

Iron-enrichment processes

Despite their unambiguous magmatic–hydrothermal origin, the processes required to form IOA deposits are still poorly understood. There are many questions that remain open, including the triggers for a magmatic system to efficiently concentrate magnetite to form an IOA deposit, the processes during magmatism that can produce these deposit types, and the primary factors that lead to the formation of large-tonnage IOA deposits. Experiments and thermodynamic modelling are key to elucidating ore-forming processes, and it is the insight from these results that is discussed in this section. Investigations of multicomponent systems with precisely controlled conditions, such as temperature, pressure, oxygen fugacity and composition, are particularly relevant as they provide reliable data necessary for obtaining robust thermodynamic parameters of minerals and

Liquidus phase
A crystalline phase that forms first on cooling from a silicate melt, at or below its liquidus temperature.

aqueous species (such as ions, complex ions and molecules). Based on such experiments, hypotheses of fractionation and accumulation of elements including Fe, P and REEs in IOA systems can be tested. Furthermore, they allow reconstruction of the source composition of melts and hydrothermal fluids, and estimation of the physico-chemical parameters relevant to ore precipitation. By contrast, thermodynamic models provide a unique method to combine data and results from experiments to make quantitative predictions about ore-forming processes leading to Fe enrichment in IOA systems.

Liquid immiscibility. Liquid immiscibility and separation of an Fe–P melt or pure Fe oxide melt has been invoked since the 1960s to explain the formation of IOA deposits. In the magmatic immiscibility model, an oxidized Fe–P-rich melt and a conjugate Si-rich melt are formed, with the subsequent intrusion and crystallization of the Fe–P-rich melt within upper crustal levels[12,17,22–24]. These processes are still debated, and other possible orthomagmatic mechanisms involve fractional crystallization and accumulation of Fe oxides from an evolved melt, as reported in layered mafic intrusions[23,55–58].

Experiments show that a phosphatic Fe-oxide melt can coexist as immiscible oxide liquids with shoshonitic melts at 900 °C and 1 GPa in the presence of carbonic vapour, magnetite and quartz; both will also form anhydrous liquids at 1,080 °C and 101 kPa (REF.[13]). Furthermore, experimentally produced immiscible melts can be highly enriched in Fe and P (33 wt% FeO_{tot}, 39 wt% P_2O_5) ± Ca (~18 wt% FeO_{tot}, ~25 wt% P_2O_5, ~30 wt% CaO), and strongly depleted in Si (<5 wt% SiO_2)[27] (FIG. 4a,b). Similar immiscible Fe–P melts have been produced in experimental investigations at temperatures from above 1,100 °C down to 600 °C, at 400 MPa (REF.[28]).

Some experimentally produced Fe–P-rich immiscible liquids might result in mineral assemblages similar to those found in some IOA deposits, such as actinolite-rich dykes and apatite-rich veins. However, these melts are in equilibrium with rhyolitic conjugates and are produced under rather oxidizing conditions (~fayalite–magnetite–quartz mineral buffer (FMQ) + 3.3). Most importantly, water preferentially partitions into the conjugate silicate melt[27], which might preclude the buoyant ascent of the dense Fe–P melt[12].

Yet, despite these constraints, liquid immiscibility cannot be completely ruled out as a mechanism for IOA formation, and further investigation is needed. Evidence that processes of assimilation, anatexis and immiscibility of carbonate–sulfate melts could be relevant to explain the formation of some IOA deposits has been found[115,148]. For example, fluid inclusion data from the Buena Vista and Iron Springs deposits in the southwestern United States and El Laco in Chile are interpreted as indicating the presence of Fe-rich carbonate–sulfate melts. These occurrences are clearly unusual and require further study to evaluate the assimilation and immiscibility hypothesis. At El Laco, evidence is still missing, as no carbonate or evaporite rocks occur at the El Laco volcanic complex[14,116], and stable isotope data unambiguously show the fingerprint of a magmatic source, precluding assimilation of evaporites[118,122]. Furthermore, mass balance calculations are needed to quantitatively evaluate whether assimilation, anatexis and immiscibility are viable mechanisms to form a large IOA deposit.

Hence, available information suggests that liquid immiscibility and formation of Fe–P (Ca) or sulfate–carbonate melts might occur on a limited scale in nature, accounting for small IOA occurrences, but probably not to produce mega- to gigatonne-scale Fe enrichment, such as Kiruna, Los Colorados or any large IOA deposit[13,165].

Flotation of igneous magnetite. In water-rich and relatively oxidized arc magmas, magnetite is a liquidus phase. It has been demonstrated experimentally that bubbles of magmatic–hydrothermal fluid nucleate on magnetite crystals with a high wetting angle, making the crystal–bubble–melt configuration energetically favourable[166,167]. The spatial association between magnetite crystals and fluid bubbles has been observed in mafic enclaves erupted in magnetite-rich andesite lavas in arc volcanoes[168] and in pumice from early-erupted rhyolites[169]. Indeed, several experimental results have presented evidence that water saturation is aided by magnetite crystals, which reduce surface energy, triggering bubble nucleation on crystal surfaces during decompression, owing to the larger wetting angles (ψ) between fluids and oxide minerals (45–50°) when compared to silicate minerals (5–25°)[170–173]. Decompression experiments at geologically relevant magmatic conditions for IOA systems have tested the efficiency of magnetite flotation in a silicate magma[174,175]. Results demonstrate that bubble–magnetite pairs can rise relative to the surrounding silicate melt, because of both the low bulk viscosity of the melt and bubble expansion, sweeping up more magnetite crystals during their ascent (FIG. 4c–d).

In terms of IOA systems, experimental data[174,175] show that the attachment of fluid bubbles to magnetite crystals could be a viable mechanism to segregate Fe from an intermediate silicate magma. In addition, the experiments[174] also demonstrate that ascending bubble–magnetite pairs coalescence and accumulate in an upper layer that grows during re-equilibration. Thus, further nucleation, growth, coalescence and accumulation of numerous bubble–magnetite pairs form a buoyant magnetite-rich hypersaline suspension on top of the magma chamber, which further becomes Fe-rich by scavenging Fe from the silicate melt[46,60].

This Fe-enrichment process is analogous to flotation mechanisms like those used in industrial ore processing[176]. Mass balance calculations[60] show its viability to form a large IOA deposit such as the Los Colorados deposit in Chile (~350 Mt Fe ore). For instance, incorporation of ~8 wt% igneous magnetite into the exsolved magmatic–hydrothermal fluid phase would decrease the magma volume required to produce ~350 Mt Fe ore in a IOA deposit from ~100 km^3 to ~50 km^3 (REFS.[46,60]). This volume is within the range of magma chambers in arc volcanoes, usually from ~4 to 60 km^3 (REF.[177]), and is consistent with estimated caldera sizes (~30 km^2) of

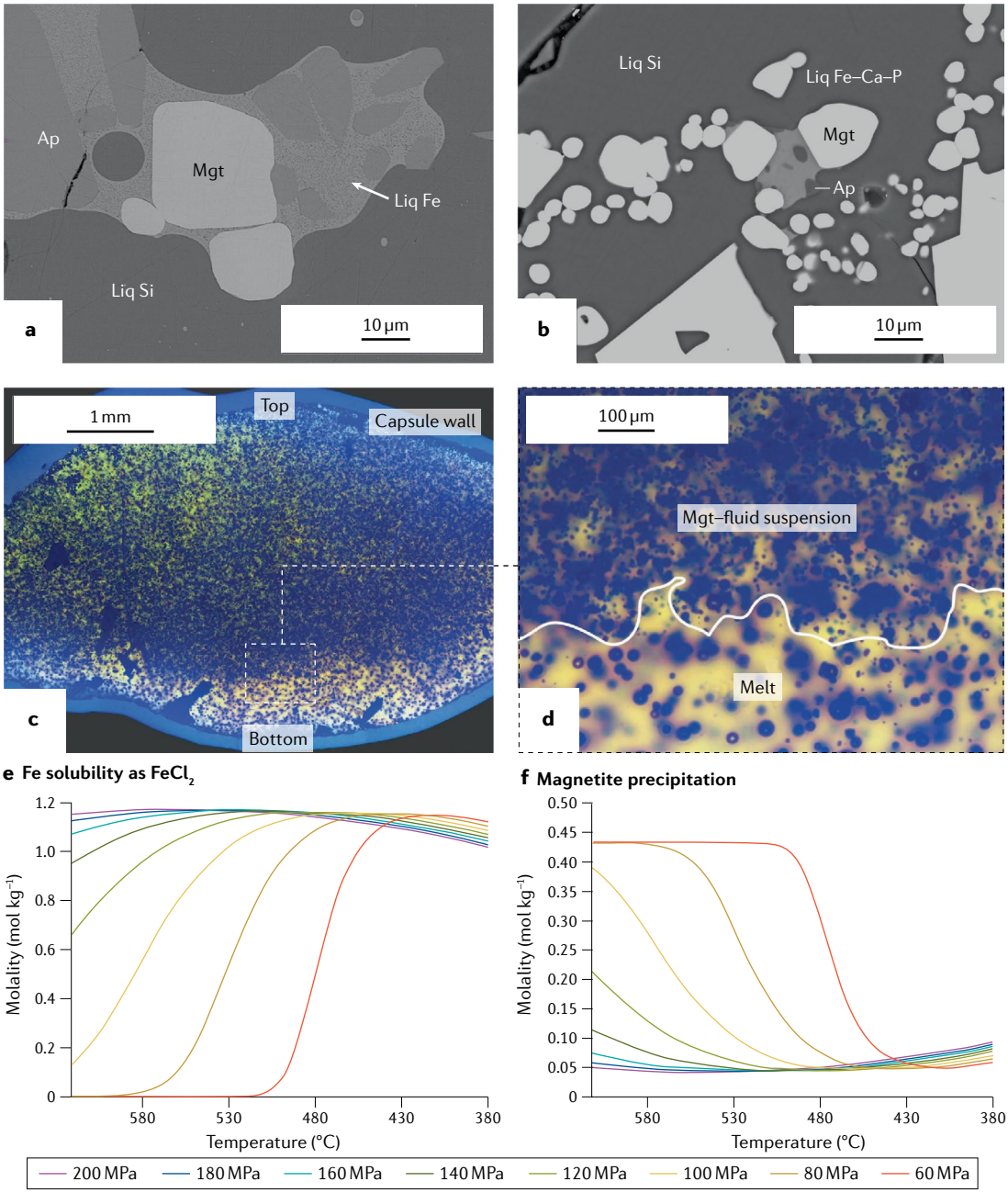

Fig. 4 | **Experimental evidence of iron-enrichment processes.** Experimental studies and thermodynamic modelling are key to elucidate Fe enrichment processes in IOA systems. **a**,**b** | Experiments show evidence of liquid (liq) immiscibility between Fe-rich (liq Fe and liq Fe–Ca–P) and Si-rich glass (liq Si). Back-scattered electron images show that magnetite (Mgt) and/or apatite (Ap) are preferentially enclosed within the immiscible Fe-rich silicate glass. **c**,**d** | Decompression experiments replicate the process of igneous magnetite flotation as a result of preferential attachment of exsolved fluid bubbles onto magnetite crystals. Transmitted light images from the $H_2O + Cl$ experiment after time $t_a = 3$ h reveal the macroscopic ascent and buoyant separation of magnetite and fluid-bubble suspensions from the residual silicate melt after decompression. **e**,**f** | Thermodynamic calculations show that the solubility of $FeCl_2$ in aqueous fluids is strongly dependent on pressure conditions, for a given temperature range (~450–620 °C). Panel **e** shows that $FeCl_2$ in the aqueous fluid decreases substantially with decreasing pressure. **f** | Model results indicate that magnetite precipitation is enhanced by rapid decompression. Panels **a** and **b** adapted from REF.[27], CC BY 4.0. Panels **c** and **d** adapted from REF.[174], CC BY 4.0. Panels **e** and **f** adapted with permission from REF.[107], Elsevier.

subvolcanic or aerial IOA deposits such as El Laco in Chile[14] and Cerro de Mercado in Mexico[63].

Note that the magnetite flotation model depends on factors that need further consideration: for example, the Fe content of the parental magma at volatile exsolution, cotectic proportions of magnetite in the melt, and physical transport aspects including mechanical entrainment of other phases such as apatite. All these aspects must be evaluated in more detail, as the model is dependent on the ability of the parental melt to produce large

amounts of magnetite. More research is needed to constrain the precise mechanisms and further assess the feasibility of magnetite flotation in magmatic systems to produce large-scale IOA deposits, including numerical simulations of magma chamber processes.

Decompression of Fe-rich aqueous fluids. Experiments have revealed that hydrothermal fluids sourced from silicate magmas are enriched in Fe over a wide pressure–temperature (*P*–*T*) range, and that the concentration of Fe is proportional to the fluid Cl contents[178–182]. Accordingly, $FeCl_2$ is expected to be the main Fe-bearing complex in highly saline supercritical hydrothermal fluids[178], and the precipitation of magnetite from this Fe–chloride complex occurs according to the reaction:

$$3\,FeCl_{2\,(aq)} + 4\,H_2O = Fe_3O_{4\,(s)} + 6\,HCl_{(aq)} + H_{2\,(aq)}$$

Experimental data at 800 °C indicate that pressure plays an important role in controlling magnetite solubility in hydrothermal fluids[181]. These results are supported by thermodynamic calculations[107], which show that magnetite solubility is strongly dependent on pressure, particularly for temperatures between ~450 and 620 °C (FIG. 4e,f), and considering a fluid salinity of 35 wt% $NaCl_{eq}$, typical of IOA systems[103]. Moreover, the model results show that the solubility of $FeCl_2$ in the hydrothermal fluid decreases substantially with decreasing pressure (FIG. 4e), triggering magnetite precipitation. The model[107] also reveals that magnetite precipitation efficiency is strongly influenced by the decompression rate. For instance, ~50% more magnetite will precipitate from a $FeCl_2$-bearing hydrothermal fluid at 600 °C and 100 MPa, compared with the amount of magnetite precipitated at 120 MPa under the same temperature (FIG. 4f). Therefore, rapid decompression of a hydrothermal fluid with a given concentration of $FeCl_2$ will improve magnetite precipitation efficiency. More detailed thermodynamic models are needed to address the effect of decompression on magnetite precipitation from hydrothermal fluids. Furthermore, other variables that promote (or inhibit) Fe transport in fluids and have an impact on massive magnetite precipitation must be explored, for example, redox conditions, presence of other volatile species and ligands.

Experiments and thermodynamic calculations show that magmatic–hydrothermal fluids could efficiently scavenge Fe from magmas to form large IOA deposits. Experimental evidence is in good agreement with mineralogical observations, trace-element data and Fe–O isotope analyses of magnetite, supporting the hypothesis that IOA deposits form from vapour-saturated intermediate magmas as a result of a specific sequence of ore-forming processes.

Towards an arc-applicable IOA model

The trace-element, isotopic and experimental data reviewed here provide a scaffold for a conceptual model that could unify the processes of IOA formation in subduction zone environments (also called arcs) under a common explanation. However, each deposit is likely to have many different magmatic and hydrothermal processes at play, which could overprint one another in multiple stages, making the initial formation conditions difficult to constrain. The conceptual model summarized in this section, which is largely based on REFS.[46,60,183], was constructed to be independent of site-specific geological attributes and attempts to unify characteristics that are common across different IOA systems. It embodies both the descriptive features and geochemical data of IOA deposits (BOX 1 and FIGS. 1–3), and an explanation of these characteristics in terms of Fe-enrichment processes (FIG. 4). It must be stressed that the processes of IOA formation will be far more complex than any descriptive model can encompass, including those discussed here, and the community should continue to test these hypotheses with further research.

Overview. The proposed conceptual model (FIG. 5) invokes the sequential operation of three distinct stages. The first relates to the crystallization of igneous magnetite in intermediate silicic magmas, a process that favours bubble nucleation (FIG. 5a). The following stage involves growth, coalescence, and accumulation of a fluid–magnetite suspension, as well as scavenging of Fe from the silicate melt into highly saline fluids (FIG. 5b). The third and final stage entails tapping of an overpressured Fe-rich fluid reservoir, allowing high-temperature magmatic–hydrothermal fluids to ascend, precipitating hydrothermal magnetite upon cooling (FIG. 5c). These processes would require optimal conditions for these steps to be met through a synergistic combination of tectono-magmatic processes.

The optimal combination of tectono-magmatic processes is broadly applicable in arc settings, which can also accommodate geological variability within and among mineralized IOA districts. However, it does not explain observations in all types of magnetite-bearing deposits, such as nelsonite-type mineralization in layered mafic intrusions[55–58], or IOA mineralization where anatectic carbonate melting has been inferred[148]. Therefore, mechanisms involving the formation of immiscible carbonate–sulfate melts generated by crustal anatexis can also have a role in forming small magnetite–apatite mineralization more commonly associated with skarn systems and carbonatite pipes[42,43].

Magnetite crystallization and volatile exsolution. In volcanic arc settings, melting of the subarc mantle is the ultimate source of intermediate magmas that pond in the upper crust (FIG. 5). In these hydrous, oxidized andesitic magma reservoirs, there is abundant evidence that magnetite segregation is a common process[168]. Primary igneous magnetite crystals form as a liquidus phase, consistent with experimental phase equilibria of mafic to intermediate silicate magmas[174,184] (FIG. 4c,d). During ascent and decompression of a magnetite-saturated intermediate magma, the decrease in solubility of the volatile components of the silicate melt (for example, H_2O or CO_2) can drive the melt to fluid saturation (FIG. 5a). This fluid saturation results in the formation of fluid-bubble–magnetite pairs during decompression-induced fluid exsolution[166,167,172]. Magnetite segregation

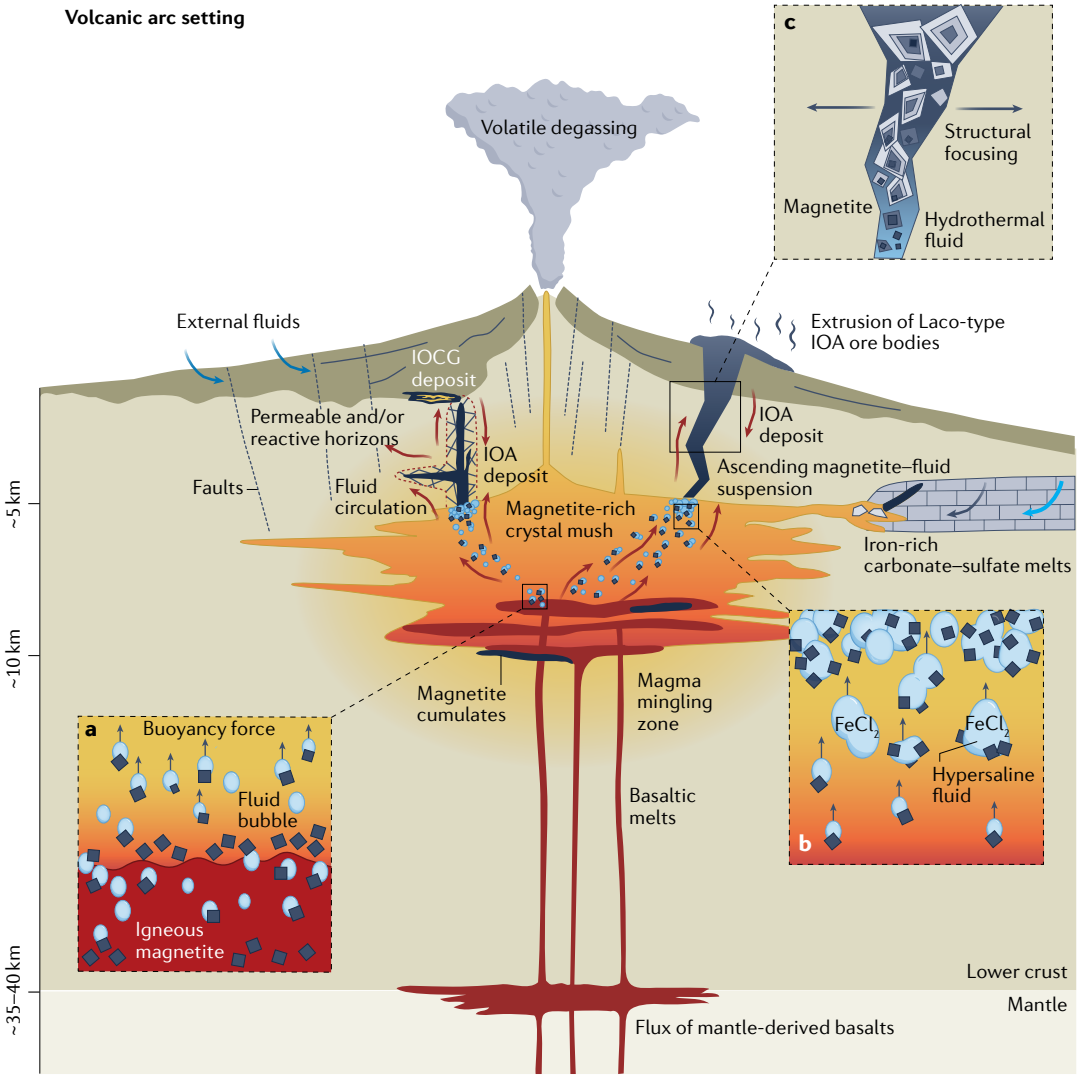

Fig. 5 | **Possible modes of IOA deposit formation in a volcanic arc setting.** Large iron oxide–apatite (IOA) deposits could form at depths of aproximately 3–5 km below the surface owing to an optimal combination of magmatic and hydrothermal processes, associated with magmatic intrusions of intermediate composition. Insets show: **a** | Ascent and decompression of a magnetite-saturated intermediate silicate melt could trigger fluid-bubble nucleation on igneous magnetite crystals. This bubble nucleation prompts the formation of bubble–magnetite pairs that rise within the magma chamber via positive buoyancy forces. **b** | The exsolved volatile phase efficiently scavenges Fe as $FeCl_2$ from the surrounding silicate melt, forming a fluid–magnetite suspension that accumulates on top of the magma chamber. **c** | Tectonic stress changes could allow the fluid–magnetite suspension to separate from the host magma through structurally enhanced pathways. The fluid–magnetite suspension would then be channelled upwards through structural weaknesses, and simultaneously, the ore fluid could continue to ascend to shallow levels, precipitating hydrothermal magnetite upon cooling. The hydrothermal ore fluid has the ability to transport Cu, Au, P, Co and rare earth elements, which can precipitate iron oxide–copper–gold (IOCG)-type mineralization at shallow or distal levels due to cooling and/or mixing with externally derived fluids. Additionally, magnetite mineralization might develop by settling into cumulate layers in the magma reservoir, and/or by formation of immiscible carbonate–sulfate melts resulting from assimilation of sedimentary rocks.

and volatile exsolution becomes more efficient owing to multiple events of recharge, marked by the injection of pulses of basaltic magma into the hydrous andesitic magma chamber[116], which can contribute to both thermal rejuvenation and enrichment in metals, chlorine and sulfur[185,186]. The magnetite budget of the magma reservoir can be further increased by transfer of micrometre- to nanometre-sized magnetite crystals and bubbles of supercritical fluid from an underplating mafic magma into the overlying andesitic reservoir (FIG. 5a). Such open-system processes have been documented in several arc volcanoes, including the Soufriere Hills volcano in Montserrat[168], and the Lascar[187] and El Laco[26] volcanoes in the Chilean Altiplano.

Magnetite and fluid accumulation. The bubble–magnetite pairs — which are fluid bubbles attached to magnetite crystals — ascend within the magma chamber owing

to positive buoyancy forces[60,168] (FIG. 5a). During decompression, the fluid component of the bubble–magnetite pairs expands and become even less dense, allowing the bubbles to entrain more magnetite crystals (FIG. 5b). The bubble–magnetite pairs coalesce and accumulate on top of the magma chamber, forming a fluid–magnetite suspension[60]. This process is supported by experimental data[174,175], which demonstrate that the attachment on fluid bubbles is strong enough to efficiently float magnetite in an intermediate silicate magma, as long as the suspension contains ≤37 vol% (or ≤65 wt%) of magnetite crystals[60], resulting in a positive buoyancy (FIG. 4c,d). During ascent, the exsolved volatile phase efficiently scavenges Fe from the surrounding silicate melt, forming $FeCl_2$ (REFS.[181,188]) (FIG. 5b), as well as other components and metals, for example, P, S, Cu, Au and REEs. Therefore, the aqueous phase of the suspension that accumulates on top of the magma chamber will be metal-rich. The presence of micro- to nano-sized igneous magnetite crystals in the magmatic–hydrothermal fluid suspension is critical for efficiently extracting Fe from a smaller body of intermediate magma, relative to formation from a conventional orthomagmatic fluid. Mass balance calculations[60] show that the incorporation of only a small proportion of igneous magnetite in the evolving ore fluid allows the formation of a IOA deposit from a relatively small volume of magma, without substantially depleting the silicate melt in Fe (REF.[46]).

It is important to note that the efficiency of the magnetite–fluid accumulation process will be strongly dependent on the volatile content of the magma, which in turn depends on pressure and depth of emplacement. Multiple lines of evidence show that magmas stored in the mid to upper crust are commonly vapour-saturated as a result of differentiation, protracted storage and mafic magma recharge[189]. In a magma reservoir zoned with respect to exsolved vapour, vapour-saturated crystallization varies from ~6 wt% near the top (~150 MPa; 4–5 km) to ~1 wt% exsolved vapour near the bottom (~250 MPa; ~8–10 km)[190]. Therefore, formation of magnetite–fluid suspensions might be a function of the depth (pressure) of magma crystallization, among other factors, with shallower magma chambers (less than ~5 km deep) favouring accumulation efficiency. By contrast, in deeper magma chambers (>5 km), conditions for optimal buoyancy of the bubble–magnetite pairs would not be met, and magnetite crystals would sink forming cumulate layers[56] at the bottom of the magma reservoir (FIG. 5).

Tapping the metal-rich fluid reservoir. Accumulation of the fluid–magnetite suspension on top of the magma chamber leads to the formation of a metal-rich fluid reservoir (FIG. 5b). Tectonic stress changes leading to regional extension and/or concentric faulting related to caldera subsidence[191] might play a major role by tapping this fluid reservoir, allowing the fluid–magnetite suspension to separate from the host magma through structural focusing (FIG. 5c). These structurally enhanced conducts or pathways include faults, fractures, brecciated host rocks, volcanic feeder zones and ring-fracture zones in caldera systems[14,46,60,78,191]. As the fluid–magnetite suspension ascends via dilatant structures, decompression and cooling lead to precipitation of hydrothermal magnetite over primary igneous magnetite crystals, which grow larger by sourcing Fe from the cooling magmatic–hydrothermal fluid (FIG. 5c). Simultaneously, the hydrothermal fluid continues to ascend to shallow levels transporting the remaining dissolved Fe, and later precipitating Fe as veins, disseminations, or massive patches of hydrothermal magnetite. This dissemination is consistent with experimental data and solubility calculations showing that rapid decompression of hydrothermal fluids favours magnetite precipitation (FIG. 4e,f). The high Cl concentration reported in IOA-forming hydrothermal fluids[92,103,115,144,148] not only enhances the solubility of Fe, but also would increase the transport efficiency of Cu, Au, P and REEs[192,193]. Therefore, the magmatic–hydrothermal ore fluid has the ability to transport these elements vertically and laterally into more distal zones, where they might precipitate IOCG-type mineralization composed of Fe oxides, Cu and Fe sulfides and phosphates by cooling[194] and/or mixing with externally derived fluids[43] (FIG. 5).

Summary and future perspectives

IOA deposits are globally distributed and formed from the Palaeoproterozoic to the Plio-Pleistocene. Despite their importance as a relevant source of Fe for modern industry, IOA deposits remained relatively little studied until the 2010s. Advances based in mineral chemistry, geochemical data and experiments have shed light on several previously unresolved questions, including how magmatic activity is related to the formation of IOA deposits, what role magmas have as a source of Fe and other metals, and how magmatic–hydrothermal fluids play a key role as agents of mineralization. The advances summarized here provide a more detailed understanding of the geological factors controlling the formation of IOA deposits and provide a framework that could help to further refine globally applicable models of IOA formation.

Mineralization temperatures span almost the whole igneous–hydrothermal spectrum, ranging from purely magmatic (~1,000–800 °C), through late magmatic and magmatic–hydrothermal (~800–600 °C), to exclusively hydrothermal (<600 °C). We suggest that externally derived fluids such as basinal brines or meteoric waters play only a limited role, and, instead, the formation of large IOA deposits is intimately linked to intermediate magmas and their exsolved high-temperature aqueous fluids. These optimal conditions for IOA mineralization are primarily met in subduction-related environments, where high-fluxing of Cl-rich hydrous basalts results from melting of the mantle wedge induced by fluids derived from sediments and devolatisation of the subducting oceanic lithosphere. Crustal thinning in extensional intra-arc and back-arc settings could allow magma ascent into the upper crust, driving some intermediate melts to become enriched in Fe by magmatic crystallization and accumulation of magnetite. Volatile saturation and formation of buoyant magnetite–fluid suspensions could then rise and accumulate on top of magma chambers, providing possible mechanisms of Fe enrichment.

Fault tapping of this metal-rich fluid reservoir would promote the rapid ascent of magmatic–hydrothermal fluids and concomitant precipitation of hydrothermal magnetite, a key factor underpinning megatonne to gigatonne-scale Fe enrichment. Additionally, other processes such as fractional crystallization, assimilation, anatexis and liquid immiscibility could account for some IOA-type mineralization occurrences. IOA deposits are highly complex, and each deposit has unique characteristics, indicating that many different magmatic and hydrothermal processes are likely to be at play, and no overall conceptual model could account for all of these individual features.

Ultimately, the processes required to form IOA deposits are poorly understood, and many fundamental questions remain. Perhaps the key question is what drives a magmatic system to efficiently concentrate magnetite to form an economic IOA deposit. There is abundant evidence that magnetite segregation is a common process in arc magmas[168,171] and in layered mafic–ultramafic intrusions[195,196]. However, most of the time the optimal conditions for massive magnetite accumulation are not met. Therefore, future work should target both fertile and barren mafic–intermediate magmatic suites to unravel the distinctive signatures diagnostic of metallogenic fertility. Research on this topic should combine petrological results of intrusive rocks coeval with IOA mineralization, including trace-element analyses and radiogenic and stable isotope determinations in whole-rock samples and accesory minerals such as zircon and apatite. These data, aimed at monitoring the evolution of the magmatic system, will provide relevant information to fingerprint the parental magma composition and crystallization conditions optimal for magnetite accumulation (for example, temperature, pressure, oxygen and sulfur fugacity). Additionally, mechanisms of P, Ti,V, Co and REE enrichment will need to be evaluated in detail by conducting further experiments and thermodynamic models.

Only a handful of researchers have explored the potential petrotectonic controls on IOA mineralization[111,197]. Their results combined geochronological and geochemical data of intrusive rocks within the Mesozoic Coastal Cordillera of northern Chile, recognizing several plutonic episodes, some of which are associated with IOA, IOCG and/or porphyry mineralization. A complex interplay between mantle, crust, slab and sediment contributions was recognized, and further research is needed to link secular changes in magmatism and (for example) crustal thickness, to periods of IOA deposit formation. Based on the global spatial and temporal distribution of IOA deposits, it is likely that the conditions of maximum efficiency to form IOA deposits are attained in more immature arcs such as the Coastal Cordillera of Chile during the Cretaceous, where the crust was thinner (<35–40 km)[111] and mafic magma fluxes were more frequent. Nevertheless, IOA deposits also form in thick crust environments (>40 km) and associated with more evolved magmatism, such as El Laco deposit in the Central Andes[14]. Therefore, it is critical to determine how crustal thickness influences melting rate and melting depth and ultimately affects the metallogenic fertility of intrusions related to IOA deposits, as has been identified for other magmatic–hydrothermal mineral systems such as porphyry Cu deposits[198]. Such efforts should be complemented by detailed research documenting the style, character and timing of deformation phases, and their importance for fluid flow and mineralizing events in volcanic plumbing systems[78,199,200].

A relevant parameter that needs to be determined is the depth of emplacement of IOA deposits, which remains poorly constrained. At present, only broad estimations are available, indicating approximate depths of formation of 3–5 km (~100–200 MPa)[107,108,111,156,158]. Thus, efforts should be made to determine palaeodepth from mineral barometers in intrusive rocks associated with IOA mineralization[201,202], in addition to structural measurements to assess the level of emplacement of IOA deposits in complexly deformed areas[78]. As decompression is a key variable controlling magnetite–fluid segregation in silicate magmas, characterization of volatiles in natural samples including melt inclusion analyses must be complemented with additional experimental data, thermodynamic models and computer simulations of magma outgassing events[203,204]. Integration of these data will be helpful to identify magma chamber processes that lead to optimal accumulation of igneous magnetite, a critical step to form IOA deposits.

The metal and non-metal content of magmatic–hydrothermal fluids associated with IOA deposits needs to be assessed in detail to determine their ore potential. Very few compositional data are available for ore-precipitating fluids in IOA systems compared to other deposit types such as porphyries[205]. Advances in near-infrared microscopy allows fluid inclusion measurements to be performed on opaque mineral phases such as Fe oxides and pyrite[206,207]. These analyses can be carried out in combination with LA-ICP-MS analyses of individual inclusions, opening opportunities for direct study of ore-forming fluids in IOA systems. In addition, mineral chemistry analyses can help bridging this gap of information. Besides magnetite and apatite, actinolite is ubiquitous in IOA deposits and bears great potential for mineral chemistry and in situ isotope results. Trace-element data for actinolite are sparse, and microtextural and compositional variations might provide further constraints on the ore-forming conditions. Such analyses would allow coupling conditions of actinolite formation in relation to magnetite and apatite mineralization, and also identifying distinct pulses of ore-forming fluids by using O–H stable isotope systematics. These analyses could further refine our understanding of the geological conditions propitious for IOA formation and their linkage to IOCG systems.

We stress that future research must determine whether IOA deposits are genetically related to IOCGs. Observations in several districts worldwide have noted a spatial relation between IOA and IOCG mineralization styles, although Fe- and Cu-rich stages are not necessarily coeval[50–54]. Constraining the timing of Fe-rich versus Cu-rich mineralization events in IOA-IOCG systems must be achieved through a combination of geochronological methods — for example, $^{40}Ar/^{39}Ar$

dating of actinolite and U–Pb dating of zircon, titanite, apatite and magnetite[45,208–211]. Such work will be critical to better understand the duration and processes that generate IOA–IOCG mineral systems, allowing for the refinement of exploration models to find new resources.

Data availability

Compilation of EMPA and LA-ICP-MS analyses of magnetite from Chilean IOA deposits is available in the online Supplementary Data file.

Published online: 13 September 2022

1. Watari, T., Nansai, K. & Nakajima, K. Major metals demand, supply, and environmental impacts to 2100: a critical review. *Resour. Conserv. Recycl.* **164**, 105107 (2021).
2. Arndt, N. T. et al. Future global mineral resources. *Geochem. Perspect*. https://doi.org/10.7185/geochempersp.6.1 (2017).
3. Morfeldt, J., Nijss, W. & Silveira, S. The impact of climate targets on future steel production — an analysis based on a global energy system model. *J. Clean. Prod.* **103**, 469–482 (2015).
4. Song, Y., Wang, N. & Yu, A. Temporal and spatial evolution of global iron ore supply-demand and trade structure. *Res. Policy* **64**, 101506 (2019).
5. Nassar, N. T. & Fortier, S. M. Methodology and technical input for the 2021 review and revision of the U.S. Critical Minerals List. Open-File Report 2021–1045, 31 (US Geological Survey, 2021).
6. Pell, R. et al. Towards sustainable extraction of technology materials through integrated approaches. *Nat. Rev. Earth Environ.* **2**, 665–679 (2021).
7. Jowitt, S. M., Mudd, G. M. & Thompson, J. F. H. Future availability of non-renewable metal resources and the influence of environmental, social, and governance conflicts on metal production. *Commun. Earth Environ.* **1**, 13 (2020).
8. Park, C. F. A magnetite 'flow' in northern Chile. *Econ. Geol.* **56**, 431–444 (1961).
9. Henriquez, F. & Martin, R. F. Crystal growth textures in magnetite flows and feeder dykes, El Laco, Chile. *Can. Mineral.* **16**, 581–589 (1978).
10. Henrîquez, F. & Nyström, J. O. Magnetite bombs at El Laco volcano, Chile. *GFF* **120**, 269–271 (1998).
11. Nyström, J. O., Henríquez, F., Naranjo, J. A. & Naslund, H. R. Magnetite spherules in pyroclastic iron ore at El Laco, Chile. *Am. Mineral.* **101**, 587–595 (2016).
12. Tornos, F., Velasco, F. & Hanchar, J. M. Iron-rich melts, magmatic magnetite, and superheated hydrothermal systems: the El Laco deposit, Chile. *Geology* **44**, 427–430 (2016).
13. Mungall, J. E., Long, K., Brenan, J. M., Smythe, D. & Naslund, H. R. Immiscible shoshonitic and Fe-P-oxide melts preserved in unconsolidated tephra at El Laco volcano, Chile. *Geology* **46**, 255–258 (2018).
14. Ovalle, J. T. et al. Formation of massive iron deposits linked to explosive volcanic eruptions. *Sci. Rep.* **8**, 14855 (2018).
15. Frietsch, R. On the magmatic origin of iron ores of the Kiruna type. *Econ. Geol.* **73**, 478–485 (1978).
16. Förster, H. & Jafarzadeh, A. The Bafq mining district in Central Iran: a highly mineralized Infracambrian volcanic field. *Econ. Geol.* **89**, 1697–1721 (1994).
17. Nyström, J. O. & Henriquez, F. Magmatic features of iron ores of the Kiruna type in Chile and Sweden; ore textures and magnetite geochemistry. *Econ. Geol.* **89**, 820–839 (1994).
18. Allen, R. L., Lundström, I., Ripa, M., Simeonov, A. & Christofferson, H. Facies analysis of a 1.9 Ga, continental margin, back-arc felsic caldera province with diverse Zn-Pb-Ag-(Cu-Au) sulphide and Fe oxide deposits, Bergslagen region, Sweden. *Econ. Geol.* **91**, 979–1008 (1996).
19. Day, W. C., Slack, J. F., Ayuso, R. A. & Seeger, C. M. Regional geologic and petrologic framework for iron oxide ± apatite ± rare earth element and iron oxide copper-gold deposits of the Mesoproterozoic St. Francois Mountains Terrane, Southeast Missouri, USA. *Econ. Geol.* **111**, 1825–1858 (2016).
20. Palma, G., Barra, F., Reich, M., Simon, A. C. & Romero, R. A review of magnetite geochemistry of Chilean iron oxide–apatite (IOA) deposits and its implications for ore-forming processes. *Ore Geol. Rev.* **126**, 103748 (2020).
21. Palma, G. et al. Thermal evolution of Andean iron oxide–apatite (IOA) deposits as revealed by magnetite thermometry. *Sci. Rep.* **11**, 18424 (2021).
22. Philpotts, A. R. Origin of certain iron-titanium oxide and apatite rocks. *Econ. Geol.* **62**, 303–315 (1967).
23. Kolker, A. Mineralogy and geochemistry of Fe-Ti oxide and apatite (Nelsonite) deposits and evaluation of the liquid immiscibility hypothesis. *Econ. Geol.* **77**, 1146–1158 (1982).
24. Naslund, H. R., Henríquez, F., Nyström, J. O., Vivallo, W. & Dobbs, F. M. in *Hydrothermal Iron Oxide Copper-Gold and Related Deposits: A Global Perspective* Vol. 2 (ed. Porter, T. M.) 207–226 (PGC, 2002).
25. Lester, G. W., Clark, A. H., Kyser, T. K. & Naslund, H. R. Experiments on liquid immiscibility in silicate melts with H_2O, P, S, F and Cl: implications for natural magmas. *Contrib. Mineral. Petrol.* **166**, 329–349 (2013).
26. Velasco, F., Tornos, F. & Hanchar, J. M. Immiscible iron- and silica-rich melts and magnetite geochemistry at the El Laco volcano (northern Chile): evidence for a magmatic origin for the magnetite deposits. *Ore Geol. Rev.* **79**, 346–366 (2016).
27. Hou, T. et al. Immiscible hydrous Fe–Ca–P melt and the origin of iron oxide-apatite ore deposits. *Nat. Commun.* **9**, 1415 (2018).
28. Lledo, H. L., Naslund, H. R. & Jenkins, D. M. Experiments on phosphate–silicate liquid immiscibility with potential links to iron oxide apatite and nelsonite deposits. *Contrib. Mineral. Petrol.* **175**, 111 (2020).
29. Bookstrom, A. A. Magmatic features of iron ores of the Kiruna type in Chile and Sweden: ore textures and magnetite geochemistry — a discussion. *Econ. Geol.* **90**, 469–475 (1995).
30. Ménard, J. J. Relationship between altered pyroxene diorite and the magnetite mineralization in the Chilean iron belt, with emphasis on the El Algarrobo iron deposits (Atacama region, Chile). *Miner. Deposita* **30**, 268–274 (1995).
31. Rhodes, A. L. & Oreskes, N. Magnetite deposition at El Laco, Chile: implications for Fe-oxide formation in magmatic-hydrothermal systems. In *Giant Ore Deposits II: Controls on the Scale of Orogenic Magmatic-Hydrothermal Mineralization*: *Proc. Second Giant Ore Deposits Workshop* (ed. Clark, A. H.) 582–622 (Department of Geological Sciences, Queen's Univ., 1995).
32. Barton, M. D. & Johnson, D. A. Evaporitic-source model for igneous-related Fe-oxide (REE–Cu–Au–U) mineralization. *Geology* **24**, 259–262 (1996).
33. Rhodes, A. L., Oreskes, N. & Sheets, R. W. Geology and REE geochemistry of the magnetite deposits at El Laco, Chile. *Econ. Geol. Spec. Publ.* **7**, 299–332 (1999).
34. Rhodes, A. L. & Oreskes, N. in *Geology and Ore Deposits of the Central Andes* 7 (ed. Skinner, B. J.) 333–351 (Society of Economic Geologists Special Publication, 1999).
35. Haynes, D. W. in *Hydrothermal Iron Oxide-Copper-Gold and Related Deposits: A Global Perspective* Vol. 1 (ed. Porter, T. M.) 71–90 (PGC, 2000).
36. Sillitoe, R. H. & Burrows, D. R. New field evidence bearing on the origin of the El Laco magnetite deposit, northern Chile. *Econ. Geol.* **97**, 1101–1109 (2002).
37. Dare, S. A. S., Barnes, S. J. & Beaudoin, G. Did the massive magnetite 'lava flows' of El Laco (Chile) form by magmatic or hydrothermal processes? New constraints from magnetite composition by LA-ICP-MS. *Miner. Deposita* **50**, 607–617 (2015).
38. Peters, S. T. M. et al. Triple oxygen isotope variations in magnetite from iron-oxide deposits, central Iran, record magmatic fluid interaction with evaporite and carbonate host rocks. *Geology* **48**, 211–215 (2020).
39. Hitzman, M. W., Oreskes, N. & Einaudi, M. T. Geological characteristics and tectonic setting of Proterozoic iron oxide (Cu–U–Au–REE) deposits. *Precam. Res.* **58**, 241–287 (1992).
40. Hitzman, M. W. in *Hydrothermal Iron Oxide Copper-Gold and Related Deposits: A Global Perspective* Vol. 1 (ed. Porter, T. M.) 9–26 (PGC, 2000).
41. Williams, P. J. et al. Iron oxide copper-gold deposits: geology, space-time distribution, and possible modes of origin. *Econ. Geol. 100th Anniv. Vol.*, 371–405 (2005).
42. Groves, D. I., Bierlein, F. P., Meinert, L. D. & Hitzman, M. W. Iron oxide copper-gold (IOCG) deposits through Earth history: implications for origin, lithospheric setting, and distinction from other epigenetic iron oxide deposits. *Econ. Geol.* **105**, 641–654 (2010).
43. Barton, M. D. in *Treatise of Geochemistry* Vol. 13 (eds. Holland, H. & Turekian, K.) 515–536 (Univ. Arizona, 2014).
44. Barra, F. et al. Unraveling the origin of the Andean IOCG clan: a Re-Os isotope approach. *Ore Geol. Rev.* **81**, 62–78 (2017).
45. Rojas, P. et al. A genetic link between magnetite mineralization and diorite intrusion at the El Romeral iron oxide-apatite deposit, northern Chile. *Miner. Deposita* **53**, 947–966.
46. Simon, A. C. et al. Kiruna-type iron oxide-apatite (IOA) and iron oxide copper-gold (IOCG) deposits form by a combination of igneous and magmatic-hydrothermal processes: evidence from the Chilean iron belt. *Soc. Econ. Geol. Spec. Pub.* **21**, 89–114 (2018).
47. Sillitoe, R. H. Iron oxide-copper-gold deposits: an Andean view. *Miner. Deposita* **38**, 787–812 (2003).
48. Espinoza, R. S., Véliz, G. H., Esquivel, L. J., Arias, F. J. & Moraga, B. A. The cupriferous province of the Coastal Range, northern Chile. In *Andean Copper Deposits: New Discoveries, Mineralization Styles and Metallogeny*, 5 (eds. Camus, F. et al.) 19–32 (Society of Economic Geologists Special Publication, 1996).
49. Reich, M. et al. Trace element signature of pyrite from the Los Colorados iron oxide-apatite (IOA) deposit, Chile: A missing link between Andean IOA and iron oxide-copper-gold systems? *Econ. Geol.* **111**, 743–761 (2016).
50. Apukhtina, O. B. et al. Early, deep magnetite-fluorapatite mineralization at the Olympic Dam Cu-U-Au-Ag deposit, South Australia. *Econ. Geol.* **112**, 1531–1542 (2017).
51. Rodriguez-Mustafa, M. A. et al. A continuum from iron oxide copper-gold to iron oxide-apatite deposits: evidence from Fe and O stable isotopes and trace element chemistry of magnetite. *Econ. Geol.* **115**, 1443–1459 (2020).
52. Verdugo-Ihl, M. R., Ciobanu, C. L., Cook, N. J., Ehrig, K. J. & Courtney-Davies, L. Defining early stages of IOCG systems: evidence from iron oxides in the outer shell of the Olympic Dam deposit, South Australia. *Miner. Deposita* **55**, 429–452 (2020).
53. Rodriguez-Mustafa, M. A. et al. The Mina Justa iron oxide copper-gold (IOCG) deposit, Peru: constraints on metal and ore fluid sources. *Econ. Geol*. https://doi.org/10.5382/econgeo.4875 (2021).
54. Skirrow, R. G. Iron oxide copper-gold (IOCG) deposits — a review (part 1): settings, mineralogy, ore geochemistry and classification. *Ore Geol. Rev.* **140**, 104569 (2022).
55. Dymek, R. & Owens, B. Petrogenesis of apatite-rich rocks (nelsonites and oxide-apatite gabbronorites) associated with massif anorthosites. *Econ. Geol.* **96**, 797–815 (2001).
56. Tegner, C., Cawthorn, R. G. & Kruger, F. J. Cyclicity in the main and upper zones of the bushveld complex, south africa: crystallization from a zoned magma sheet. *J. Petrol.* **47**, 2257–2279 (2006).
57. Tollari, N., Barnes, S.-J., Cox, R. A. & Nabil, H. Trace element concentrations in apatites from the Sept-Îles Intrusive Suite, Canada — implications for the genesis of nelsonites. *Chem. Geol.* **252**, 180–190 (2008).
58. Charlier, B. et al. The Grader layered intrusion (Havre-Saint-Pierre anorthosite, Quebec) and genesis of nelsonite and other Fe-Ti-P ores. *Lithos* **101**, 359–378 (2008).
59. Treloar, P. J. & Colley, H. Variations in F and Cl contents in apatites from magnetite-apatite ores in northern Chile, and their ore-genetic implications. *Mineral. Mag.* **60**, 285–301 (1996).
60. Knipping, J. L. et al. Giant Kiruna-type deposits form by efficient flotation of magmatic magnetite suspensions. *Geology* **43**, 591–594 (2015).
61. Zhang, Z. et al. Spatio-temporal distribution and tectonic settings of the major iron deposits in China: an overview. *Ore Geol. Rev.* **57**, 247–263 (2014).
62. Taylor, R. D., Shah, A. K., Walsh, G. J. & Taylor, C. D. Geochemistry and geophysics of iron oxide-apatite (IOA) deposits and associated waste piles with

implications for potential rare earth element (REE) resources from ore and historic mine waste in the eastern Adirondack Highlands, New York, USA. *Econ. Geol.* **114**, 1569–1598 (2019).
63. Lyons, J. I. Volcanogenic iron oxide deposits, Cerro de Mercado and vicinity, Durango, Mexico. *Econ. Geol.* **83**, 1886–1906 (1988).
64. Chen, H. et al. Evolution of the Giant Marcona-Mina Justa iron oxide-copper-gold district, south-central Peru. *Econ. Geol.* **105**, 155–185 (2010).
65. Corriveau, L., Montreuil, J.-F. & Potter, E. G. Alteration facies linkages among iron oxide copper-gold, iron oxide-apatite, and affiliated deposits in the Great Bear magmatic zone, Northwest Territories, Canada. *Econ. Geol.* **111**, 2045–2072 (2016).
66. Ootes, L. et al. A Paleoproterozoic Andean-type iron oxide copper-gold environment, the Great Bear magmatic zone, Northwest Canada. *Ore Geol. Rev.* **81**, 123–139 (2017).
67. Helvaci, C. Apatite-rich iron deposits of the Avnik (Bingol) region, southeastern Turkey. *Econ. Geol.* **79**, 354–371 (1984).
68. He, X. F., Santosh, M., Tsunogae, T. & Malaviarachchi, S. P. K. Magnetite-apatite deposit from Sri Lanka: implications on Kiruna-type mineralization associated with ultramafic intrusion and mantle metasomatism. *Am. Mineral.* **103**, 26–38 (2018).
69. Seo, J., Choi, S. G., Kim, D. W., Park, J. W. & Oh, C. W. A new genetic model for the Triassic Yangyang iron-oxide-apatite deposit, South Korea: constraints from in situ U-Pb and trace element analyses of accessory minerals. *Ore Geol. Rev.* **70**, 110–135 (2015).
70. Sun, W. et al. Geochronology and geochemistry of the Fe ore-bearing Zhonggu intrusions of the Ningwu basin: implications for tectonic setting and contemporaneous Cu-Au mineralization in the Middle–Lower Yangzte Metallogenic Belt. *Ore Geol. Rev.* **84**, 246–272 (2017).
71. Sun, W. et al. In situ LA–ICP–MS trace element analyses of magnetite: genetic implications for the Zhonggu orefield, Ningwu volcanic basin, Anhui Province, China. *Miner. Deposita* **54**, 1243–1264 (2019).
72. Parak, T. Kiruna iron ores are not intrusive-magmatic ores of the Kiruna type. *Econ. Geol.* **70**, 1242–1258 (1975).
73. Romer, R., Martinsson, O. & Perdahl, J. Geochronology of the Kiruna iron ores and hydrothermal alterations. *Econ. Geol.* **89**, 1249–1261 (1994).
74. Martinsson, O. Geology and metallogeny of the Northern Norrbotten Fe-Cu-Au province. *Soc. Econ. Geol. Guideb. Ser.* **33**, 131–148 (2004).
75. Westhues, A., Hanchar, J. M., Whitehouse, M. J. & Martinsson, O. New constraints on the timing of host-rock emplacement, hydrothermal alteration, and iron oxide-apatite mineralization in the Kiruna district, Norrbotten, Sweden. *Econ. Geol.* **111**, 1595–1618 (2016).
76. Westhues, A., Hanchar, J. M., LeMessurier, M. & Whitehouse, M. J. Evidence for hydrothermal alteration and source regions for the Kiruna iron oxide-apatite ore (northern Sweden) from zircon Hf and O isotopes. *Geology* **45**, 571–574 (2017).
77. Westhues, A. et al. Tracing the fluid evolution of the Kiruna iron oxide apatite deposits using zircon, monazite, and whole rock trace elements and isotopic studies. *Chem. Geol.* **466**, 303–322 (2017).
78. Andersson, J. B. H., Bauer, T. E. & Martinsson, O. Structural evolution of the Central Kiruna Area, Northern Norrbotten, Sweden: implications on the geologic setting generating iron oxide-apatite and epigenetic iron and copper sulfides. *Econ. Geol.* **116**, 1981–2009 (2021).
79. Jonsson, E. et al. Magmatic origin of giant 'Kiruna-type' apatite-iron-oxide ores in Central Sweden. *Sci. Rep.* **3**, 1644 (2013).
80. Jonsson, E., Harlov, D. E., Majka, J., Högdahl, K. & Persson-Nilsson, K. Fluorapatite-monazite-allanite relations in the Grängesberg apatite-iron oxide ore district, Bergslagen, Sweden. *Am. Mineral.* **101**, 1769–1782 (2016).
81. Slack, J. F., Corriveau, L. & Hitzman, M. W. A special issue devoted to proterozoic iron oxide-apatite (±REE) and iron oxide copper-gold and affiliated deposits of Southeast Missouri, USA, and the Great Bear Magmatic Zone, Northwest Territories, Canada: Preface. *Econ. Geol.* **111**, 1803–1814 (2016).
82. Nold, J. L., Dudley, M. A. & Davidson, P. The southeast Missouri (USA) Proterozoic iron metallogenic province — types of deposits and genetic relationships to magnetite-apatite and iron oxide-copper-gold deposits. *Ore Geol. Rev.* **57**, 154–171 (2014).
83. Day, W. C. & Granitto, M. Geologic field notes and geochemical analyses of outcrop and drill core from Mesoproterozoic rocks and iron-oxide deposits and prospects of southeast Missouri. Open-File Report 2014-1053 (USGS, 2014).
84. Childress, T. M., Simon, A. C., Day, W. C., Lundstrom, C. C. & Bindeman, I. N. Iron and oxygen isotope signatures of the Pea Ridge and Pilot Knob magnetite-apatite deposits, Southeast Missouri, USA. *Econ. Geol.* **111**, 2033–2044 (2016).
85. Nold, J. L., Davidson, P. & Dudley, M. A. The Pilot Knob magnetite deposit in the Proterozoic St. Francois Mountains terrane, southeast Missouri, USA: a magmatic and hydrothermal replacement iron deposit. *Ore Geol. Rev.* **53**, 446–469 (2013).
86. Mercer, C. N., Watts, K. E. & Gross, J. Apatite trace element geochemistry and cathodoluminescent textures — a comparison between regional magmatism and the Pea Ridge IOA-REE and Boss IOCG deposits, southeastern Missouri iron metallogenic province, USA. *Ore Geol. Rev.* **116**, 103129 (2020).
87. Watts, K. E. & Mercer, C. N. Zircon-hosted melt inclusion record of silicic magmatism in the Mesoproterozoic St. Francois Mountains terrane, Missouri: origin of the Pea Ridge iron oxide-apatite-rare earth element deposit and implications for regional crustal pathways of mineralization. *Geochim. Cosmochim. Acta* **272**, 54–77 (2020).
88. Tunnell et al. The Pilot Knob iron ore deposits in southeast Missouri, USA: a high-to-low temperature magmatic-hydrothermal continuum. *Ore Geol. Rev.* **131**, 103973 (2021).
89. Aleinikoff, J. N. et al. U-Pb, Re-Os, and Ar/Ar geochronology of rare earth element (REE)-rich breccia pipes and associated host rocks from the Mesoproterozoic Pea Ridge Fe-REE-Au deposit, S. Francois Mountains, Missouri. *Econ. Geol.* **111**, 1883–1914 (2016).
90. Neymark, L. A. et al. High spatial resolution U-Pb geochronology and Pb isotope geochemistry of magnetite-apatite ore from the Pea Ridge iron oxide-apatite deposit, St. Francois Mountains, southeast Missouri, USA. *Econ. Geol.* **111**, 1915–1933 (2016).
91. Ayuso, R. A., Slack, J. F., Day, W. C. & McCafferty, A. E. Geochemistry, Nd-Pb isotopes, and Pb-Pb ages of Mesoproterozoic Pea Ridge iron oxide-apatite-rare earth element deposit, southeast Missouri. *Econ. Geol.* **111**, 1935–1962 (2016).
92. Hofstra, A. H. et al. Mineral thermometry and fluid inclusion studies of the Pea Ridge iron oxide-apatite-rare earth element deposit, Mesoproterozoic St. Francois Mountains Terrane, Southeast Missouri, USA. *Econ. Geol.* **111**, 1985–2016 (2016).
93. Daliran, F. in *Hydrothermal Iron Oxide-Copper-Gold and Related Deposits: A Global Perspective* Vol. 2 (ed. Porter, T. M.) 303–320 (PGC, 2002).
94. Torab, F. M. & Lehmann, B. Magnetite-apatite deposits of the Bafq district, Central Iran: apatite geochemistry and monazite geochronology. *Mineral. Mag.* **71**, 347–363 (2007).
95. Mokhtari, M. A. A., Zadeh, G. H. & Emami, M. H. Genesis of iron-apatite ores in Posht-e-Badam Block (Central Iran) using REE geochemistry. *J. Earth Syst. Sci.* **122**, 795–807 (2013).
96. Heidarian, H., Alirezaei, S. & Lentz, D. R. Chadormalu Kiruna-type magnetite-apatite deposit, Bafq district, Iran: insights into hydrothermal alteration and petrogenesis from geochemical, fluid inclusion, and sulfur isotope data. *Ore Geol. Rev.* **83**, 43–62 (2017).
97. Heidarian, H., Lentz, D., Alirezaei, S., McFarlane, C. & Peighambari, S. Multiple stage ore formation in the Chadormalu Iron Deposit, Bafq Metallogenic Province, Central Iran: evidence from BSE imaging and apatite EPMA and LA-ICP-MS U-Pb geochronology. *Minerals* **8**, 87 (2018).
98. Ziapour, S., Esmaeily, D., Khoshnoodi, K., Niroomand, S. & Simon, A. C. Mineralogy, geochemistry, and genesis of the Chahgaz (XIVA anomaly) Kiruna-type iron oxide-apatite (IOA) deposit, Bafq district, Central Iran. *Ore Geol. Rev.* **128**, 103924 (2021).
99. Stosch, H. G., Romer, R. L., Daliran, F. & Rhede, D. Uranium–lead ages of apatite from iron oxide ores of the Bafq District, east-central Iran. *Miner. Deposita* **46**, 9–21 (2011).
100. Nayebi, N., Esmaeily, D., Chew, D. M., Lehmann, B. & Modabberi, S. Geochronological and geochemical evidence for multi-stage apatite in the Bafq iron metallogenic belt (central Iran), with implications for the Chadormalu iron-apatite deposit. *Ore Geol. Rev.* **132**, 104054 (2021).
101. Chen, H., Clark, A. H. & Kyser, T. K. The Marcona magnetite deposit, Ica, south-central Peru: a product of hydrous, iron oxide-rich melts? *Econ. Geol.* **105**, 1441–1456 (2010).
102. Oyarzún, R., Oyarzún, J., Mênard, J. J. & Lillo, J. The Cretaceous iron belt of northern Chile: role of oceanic plates, a superplume event, and a major shear zone. *Miner. Deposita* **38**, 640–646 (2003).
103. Knipping, J. L. et al. Trace elements in magnetite from massive iron oxide–apatite deposits indicate a combined formation by igneous and magmatic-hydrothermal processes. *Geochim. Cosmochim. Acta* **171**, 15–38 (2015).
104. Knipping, J. L. et al. In-situ iron isotope analyses reveal igneous and magmatic-hydrothermal growth of magnetite at the Los Colorados Kiruna-type iron oxide–apatite deposit, Chile. *Am. Mineral.* **104**, 471–484 (2019).
105. La Cruz, N. L. et al. The geochemistry of apatite from the Los Colorados iron oxide–apatite deposit, Chile: implications for ore genesis. *Miner. Deposita* **54**, 1143–1156 (2019).
106. Bookstrom, A. A. The magnetite deposits of El Romeral, Chile. *Econ. Geol.* **72**, 1101–1130 (1977).
107. Rojas, P. et al. New contributions to the understanding of Kiruna-type iron oxide–apatite deposits revealed by magnetite ore and gangue mineral geochemistry at the El Romeral deposit, Chile. *Ore Geol. Rev.* **93**, 413–435 (2018).
108. Salazar, E. et al. Trace element geochemistry of magnetite from the Cerro Negro Norte iron oxide–apatite deposit, northern Chile. *Miner. Deposita* **55**, 409–428 (2020).
109. Gelcich, S., Davis, D. W. & Spooner, E. T. C. Testing the apatite-magnetite geochronometer: U-Pb and $^{40}Ar/^{39}Ar$ geochronology of plutonic rocks, massive magnetite-apatite tabular bodies, and IOCG mineralization in Northern Chile. *Geochim. Cosmochim. Acta* **69**, 3367–3384 (2005).
110. Palma, G. et al. Halogens, trace element concentrations, and Sr-Nd isotopes in apatite from iron oxide–apatite (IOA) deposits in the Chilean iron belt: evidence for magmatic and hydrothermal stages of mineralization. *Geochim. Cosmochim. Acta* **246**, 515–540 (2019).
111. Jara, J. J. et al. Episodic construction of the early Andean Cordillera unravelled by zircon petrochronology. *Nat. Commun.* **12**, 4930 (2021).
112. Naranjo, J. A., Henríquez, F. & Nyström, J. O. Subvolcanic contact metasomatism at El Laco Volcanic Complex, Central Andes. *Andean Geol.* **37**, 110–120 (2010).
113. Tornos, F., Velasco, F. & Hanchar, J. M. The magmatic to magmatic-hydrothermal evolution of the El Laco deposit (Chile) and its implications for the genesis of magnetite-apatite deposits. *Econ. Geol.* **112**, 1595–1628 (2017).
114. Xie, Q. et al. New insights for the formation of Kiruna-type iron deposits by immiscible hydrous Fe-P Melt and high-temperature hydrothermal processes: evidence from El Laco deposit. *Econ. Geol.* **114**, 35–46 (2019).
115. Bain, W. M. et al. Evidence for iron-rich sulfate melt during magnetite(-apatite) mineralization at El Laco, Chile. *Geology* **49**, 1044–1048 (2021).
116. Ovalle, J. T. et al. Magmatic-hydrothermal evolution of the El Laco iron deposit revealed by trace element geochemistry and high-resolution chemical mapping of magnetite assemblages. *Geochim. Cosmochim. Acta* https://doi.org/10.1016/j.gca.2022.03.012 (2022).
117. Broughm, S. G., Hanchar, J. M., Tornos, F., Westhues, A. & Attersley, S. Mineral chemistry of magnetite from magnetite-apatite mineralization and their host rocks: examples from Kiruna, Sweden, and El Laco, Chile. *Miner. Deposita* **52**, 1223–1244 (2017).
118. Childress, T. et al. Triple oxygen, hydrogen, and iron stable isotope signatures indicate a silicate magma source and magmatic- hydrothermal genesis for magnetite orebodies at El Laco, Chile. *Econ. Geol.* **115**, 1519–1536 (2020).
119. La Cruz, N. L. et al. The geochemistry of magnetite and apatite from the El Laco iron oxide–apatite deposit, Chile: implications for ore genesis. *Econ. Geol.* **115**, 1461–1491 (2020).
120. Huang, X. W. & Beaudoin, G. Textures and chemical compositions of magnetite from iron oxide copper-gold (IOCG) and Kiruna-type iron oxide-apatite (IOA) deposits and their implications for ore genesis and magnetite classification schemes. *Econ. Geol.* **114**, 1–74 (2019).

121. Huang, X. W. et al. Trace element composition of iron oxides from IOCG and IOA deposits: relationship to hydrothermal alteration and deposit subtypes. *Miner. Deposita* **54**, 525–552 (2019).
122. Bilenker, L. D. et al. Fe-O stable isotope pairs elucidate a high-temperature origin of Chilean iron oxide-apatite deposits. *Geochim. Cosmochim. Acta* **177**, 94–104 (2016).
123. Troll, V. R. et al. Global Fe–O isotope correlation reveals magmatic origin of Kiruna-type apatite-iron-oxide ores. *Nat. Commun.* **10**, 1712 (2019).
124. Ghiorso, M. S. & Sack, O. Fe–Ti oxide geothermometry: thermodynamic formulation and the estimation of intensive variables in silicic magmas. *Contrib. Mineral. Petrol.* **108**, 485–510 (1991).
125. Dare, S. A. et al. Trace elements in magnetite as petrogenetic indicators. *Miner. Deposita* **49**, 785–796 (2014).
126. Sievwright, R. H., Wilkinson, J. J., O'Neill, H. S. C. & Berry, A. J. Thermodynamic controls on element partitioning between titanomagnetite and andesitic–dacitic silicate melts. *Contrib. Mineral. Petrol.* **172**, 62 (2017).
127. Sievwright, R. H., O'Neill, H. S. C., Tolley, J., Wilkinson, J. J. & Berry, A. J. Difusion and partition coefcients of minor and trace elements in magnetite as a function of oxygen fugacity at 1150 °C. *Contrib. Mineral. Petrol.* **175**, 40 (2020).
128. Dupuis, C. & Beaudoin, G. Discriminant diagrams for iron oxide trace element fingerprinting of mineral deposit types. *Miner. Deposita* **46**, 319–335 (2011).
129. Nadoll, P., Mauk, J. L., Hayes, T. S., Koenig, A. E. & Box, S. E. Geochemistry of magnetite from hydrothermal ore deposits and host rocks of the Mesoproterozoic Belt Supergroup, United States. *Econ. Geol.* **107**, 1275–1292 (2012).
130. Nadoll, P., Angerer, T., Mauk, J. L., French, D. & Walshe, J. The chemistry of hydrothermal magnetite: a review. *Ore Geol. Rev.* **61**, 1–32 (2014).
131. Nadoll, P., Mauk, J. L., Leveille, R. A. & Koenig, A. E. Geochemistry of magnetite from porphyry Cu and skarn deposits in the southwestern United States. *Miner. Deposita* **50**, 493–515 (2015).
132. Deditius, A. P. et al. Nanogeochemistry of hydrothermal magnetite. *Contrib. Miner. Petrol.* **173**, 46 (2018).
133. Canil, D. & Lacourse, T. Geothermometry using minor and trace elements in igneous and hydrothermal magnetite. *Chem. Geol.* **541**, 119576 (2020).
134. Verdugo-Ihl, M. R. et al. Nanomineralogy of hydrothermal magnetite from Acropolis, South Australia: genetic implications for iron-oxide copper gold mineralization. *Am. Mineral.* **106**, 1273–1293 (2021).
135. Huang, X. W. & Beaudoin, G. Nanoinclusions in zoned magnetite from the Sossego IOCG deposit, Carajás, Brazil: implication for mineral zoning and magnetite origin discrimination. *Ore Geol. Rev.* **139**, 104453.
136. Hu, H. et al. Reequilibration processes in magnetite from iron skarn deposits. *Econ. Geol.* **111**, 1–8 (2015).
137. Wen, G. et al. Hydrothermal reequilibration of igneous magnetite in altered granitic plutons and its implications for magnetite classification schemes: insights from the Handan-Xingtai iron district, North China Craton. *Geochim. Cosmochim. Acta* **213**, 255–270 (2017).
138. Yin, S., Ma, C. & Robinson, P. T. Textures and high field strength elements in hydrothermal magnetite from a skarn system: Implications for coupled dissolution-reprecipitation reactions. *Am. Mineral.* **102**, 1045–1056 (2017).
139. Liu, Y. et al. In-situ LA-ICP-MS trace element analysis of magnetite from Mesozoic iron oxide apatite (IOA) deposits in the Luzong volcanic basin, eastern China. *J. Asian Earth Sci.* **166**, 233–246 (2018).
140. Krolop, P. et al. Trace element geochemistry of iron oxides from the Per Geijer apatite iron ores in the Kiruna district, northern Sweden: implications for ore genesis. EGU21-1987 (EGU General Assembly, 2021).
141. Majidi, S. A. et al. Employing geochemistry and geochronology to unravel genesis and tectonic setting of iron oxide-apatite deposits of the Bafq-Saghand metallogenic belt, Central Iran. *Int. J. Earth. Sci.* **110**, 127–164 (2021).
142. Sidder, G. B. et al. Mineralogic and fluid-inclusion studies of the Pea Ridge iron-rare-earth-element deposit, southeast Missouri. *USGS Bull.* **2039**, 205–216 (1993).
143. Sheets, S. A. *Fluid Inclusion Study of the El Laco Magnetite Deposits, Chile*. MSc thesis, 94 (Dartmouth College, Hanover, 1997).
144. Broman, C., Nyström, J. O., Henríquez, F. & Elfman, M. Fluid inclusions in magnetite-apatite ore from a cooling magmatic system at El Laco, Chile. *GFF* **121**, 253–267 (1999).
145. Jami, M., Dunlop, A. C. & Cohen, D. R. Fluid inclusion and stable isotope study of Esfordi apatite-magnetite deposit, Central Iran. *Econ. Geol.* **102**, 1111–1125 (2007).
146. Gleeson, S. A. & Smith, M. P. The sources and evolution of mineralizing fluids in iron oxide-copper-gold systems, Norrbotten, Sweden: constraints from Br/Cl ratios and stable Cl isotopes of fluid inclusion leachates. *Geochim. Cosmochim. Acta* **73**, 5658–5672 (2009).
147. Martinsson, O., Billström, K., Broman, C., Weihed, P. & Wanhainen, C. Metallogeny of the Northern Norrbotten Ore Province, northern Fennoscandian Shield with emphasis on IOCG and apatite-iron ore deposits. *Ore Geol. Rev.* **78**, 447–492 (2016).
148. Bain, W. M. et al. A fundamental role of carbonate–sulfate melts in the formation of iron oxide–apatite deposits. *Nat. Geosci.* **13**, 751–757 (2020).
149. Harlov, D. E. et al. Apatite–monazite relations in the Kiirunavaara magnetite–apatite ore, northern Sweden. *Chem. Geol.* **191**, 47–72 (2002).
150. Xie, Q. H. et al. Magnesium isotopic composition of continental arc andesites and the implications: A case study from the El Laco volcanic complex, Chile. *Lithos* **318–319**, 91–103 (2018).
151. Lledo, H. L. & Jenkins, D. M. Experimental investigation of the upper thermal stability of Mg-rich actinolite; implications for Kiruna-type iron deposits. *J. Petrol.* **49**, 225–238 (2008).
152. Nyström, J. O. et al. Oxygen isotope composition of magnetite in iron ores of the Kiruna type in Chile and Sweden. *GFF* **130**, 177–188 (2008).
153. Johnson, C. A., Day, W. C. & Rye, R. O. Oxygen, hydrogen, sulfur, and carbon isotopes in the Pea Ridge magnetite-apatite deposit, southeast Missouri, and sulfur isotope comparisons to other iron deposits in the region. *Econ. Geol.* **111**, 2017–2032 (2016).
154. Deymar, S., Yazdi, M., Rezvanianzadeh, M. R. & Behzadi, M. Alkali metasomatism as a process for Ti–REE–Y–U–Th mineralization in the Saghand Anomaly 5, Central Iran: insights from geochemical, mineralogical, and stable isotope data. *Ore Geol. Rev.* **93**, 308–336 (2018).
155. Xie, Q. et al. Constraints of Fe-O isotopes on the origin of magnetite in the El Laco Kiruna-type iron deposit, Chile. *Ore Geol. Rev.* **130**, 103967 (2021).
156. McCafferty, A. E., Phillips, J. D., Hofstra, A. H. & Day, W. C. Crustal architecture beneath the southern midcontinent (USA) and controls on Mesoproterozoic iron-oxide mineralization from 3D geophysical models. *Ore Geol. Rev.* **111**, 102966 (2019).
157. Shah, A. K., Taylor, R. D., Walsh, G. & Phillips, J. Integrated geophysical imaging of rare-earth-element-bearing iron oxide-apatite deposits in the eastern Adirondack Highlands, New York. *Geophysics* **86**, B37–B54 (2021).
158. Hildebrand, R. S. Kiruna-type deposits: their origin and relationship to intermediate subvolcanic plutons in the Great Bear Magmatic Zone, Northwest Canada. *Econ. Geol.* **81**, 640–659 (1986).
159. Camprubí, A. et al. Geochronology of Mexican mineral deposits. VII: The Peña Colorada magmatic-hydrothermal iron oxide deposits (IOCG 'clan'), Colima. *Bol. Soc. Geol. Mex.* **70**, 633–674 (2018).
160. Heimann, A., Beard, B. L. & Johnson, C. M. The role of volatile exsolution and sub-solidus fluid/rock interactions in producing high $^{56}Fe/^{54}Fe$ ratios in siliceous igneous rocks. *Geochim. Cosmochim. Acta* **72**, 4379–4396 (2008).
161. Bindeman, I. Oxygen isotopes in mantle and crustal magmas as revealed by single crystal analysis. *Rev. Mineral. Geochem.* **69**, 445–478 (2008).
162. Weis, F. *Oxygen and Iron Isotope Systematics of the Grängesberg Mining District (GMD), Central Sweden*. MSc thesis, 77 (Uppsala Univ., 2013).
163. Tornos, F., Hanchar, J. M., Munizaga, R., Velasco, F. & Galindo, C. The role of the subducting slab and melt crystallization in the formation of magnetite-(apatite) systems, Coastal Cordillera of Chile. *Miner. Deposita* **56**, 253–278 (2021).
164. Weis, F. et al. Absence of hydrothermal oxygen isotope variations in host rocks supports magmatic origin of the giant Grängesberg iron oxide–apatite (IOA) deposit, Central Sweden. *Int. J. Earth. Sci.* https://doi.org/10.1007/s00531-021-02122-9 (2021).
165. Lindsley, D. H. & Epler, N. Do Fe-Ti-oxide magmas exist? Probably not! *Am. Mineral.* **102**, 2157–2169 (2017).
166. Hurwitz, S. & Navon, O. Bubble nucleation in rhyolitic melts: experiments at high pressure, temperature, and water content. *Earth Planet. Sci. Let.* **122**, 267–280 (1994).
167. Gardner, J. E. & Denis, M. H. 2004, Heterogeneous bubble nucleation on Fe-Ti oxide crystals in high-silica rhyolitic melts. *Geochim. Cosmochim. Acta* **68**, 3587–3597 (2004).
168. Edmonds, M., Brett, A., Herd, R. A., Humphreys, M. C. S. & Woods, A. Magnetite-bubble aggregates at mixing interfaces in andesite magma bodies. *Geol. Lond. Spec. Publ.* **410**, 95–121 (2014).
169. Gualda, G. A. R. & Anderson, A. T. Magnetite scavenging and the buoyancy of bubbles in magmas. Part 1: Discovery of a pre-eruptive bubble in Bishop rhyolite. *Contrib. Mineral. Petrol.* **154**, 733–742 (2007).
170. Gardner, J. E. Heterogeneous bubble nucleation in highly viscous silicate melts during instantaneous decompression from high pressure. *Chem. Geol.* **236**, 1–12 (2007).
171. Gualda, G. A. R. & Ghiorso, M. S. Magnetite scavenging and the buoyancy of bubbles in magmas. Part 2: Energetics of crystal-bubble attachment in magmas. *Contrib. Miner. Petrol.* **154**, 479–490 (2007).
172. Cluzel, N., Laporte, D. & Provost, A. Kinetics of heterogeneous bubble nucleation in rhyolitic melts: implications for the number density of bubbles in volcanic conduits and for pumice textures. *Contrib. Miner. Petrol.* **156**, 745–763 (2008).
173. Gardner, J. E. & Ketcham, R. A. Bubble nucleation in rhyolite and dacite melts: temperature dependence of surface tension. *Contrib. Miner. Petrol.* **162**, 929–943 (2011).
174. Knipping, J. L., Webster, J. D., Simon, A. C. & Holtz, F. Accumulation of magnetite by flotation on bubbles during decompression of silicate magma. *Sci. Rep.* **9**, 3852 (2019).
175. Plêse, P. et al. Production and detachment of oxide crystal shells on bubble walls during experimental vesiculation of andesitic magmas. *Contrib. Miner. Petrol.* **174**, 21 (2019).
176. Edmonds, M. Flotation of magmatic minerals. Research focus. *Geology* **43**, 655–656 (2015).
177. Townsend, M. & Huber, C. A critical magma chamber size for volcanic eruptions. *Geology* **48**, 431–435 (2020).
178. Chou, I. M. & Eugster, H. P. Solubility of magnetite in supercritical chloride solutions. *Am. J. Sci.* **277**, 1296–1314 (1977).
179. Heinrich, C. A., Ryan, C. G., Mernagh, T. P. & Eadington, P. J. Segregation of ore metals between magmatic brine and vapor — a fluid inclusion study using PIXE microanalysis. *Econ. Geol.* **87**, 1566–1583 (1992).
180. Audétat, A., Günther, D. & Heinrich, C. A. Magmatic-hydrothermal evolution in a fractionating granite: a micro-chemical study of the Sn-W-F-mineralized mole granite (Australia). *Geochim. Cosmochim. Acta* **64**, 3373–3393 (2000).
181. Simon, A. C., Pettke, T., Candela, P. A., Piccoli, P. M. & Heinrich, A. H. Magnetite solubility and iron transport in magmatic-hydrothermal environments. *Geochim. Cosmochim. Acta* **68**, 4905–4914 (2004).
182. Williams-Jones, A. E. & Heinrich, C. A. Vapor transport of metals and the formation of magmatic-hydrothermal ore deposits. *Econ. Geol.* **100**, 1287–1312 (2005).
183. Matveev, S. & Ballhaus, C. Role of water in the origin of podiform chromitite deposits. *Earth Planet. Sci. Lett.* **203**, 235–243 (2002).
184. Martel, C., Pichavant, M., Holtz, F. & Scaillet, B. Effects of fO_2 and H_2O on andesite phase relations between 2 and 4 kbar. *J. Geophys. Res.* **104**, 29453–29470 (1999).
185. Mungall, J. E., Brenan, J. M., Godel, B., Barnes, S. & Gaillard, F. Transport of metals and sulphur in magmas by flotation of sulphide melt on vapour bubbles. *Nat. Geosci.* **8**, 216–219 (2015).
186. Cashman, C. V., Sparks, R. J. S. & Blundy, J. D. Vertically extensive and unstable magmatic systems: a unified view of igneous processes. *Science* **355**, 6331 (2017).
187. Matthews, S. J., Sparks, R. S. J. & Gardeweg, M. C. The Piedras Grandes–Soncor Eruptions, Lascar Volcano, Chile; evolution of a zoned magma chamber in the Central Andean upper crust. *J. Petrol.* **40**, 1891–1919 (1999).
188. Bell, A. & Simon, A. C. Evidence for the alteration of the $Fe^{3+}/\Sigma Fe$ of silicate melt caused by the degassing of chlorine-bearing aqueous volatiles. *Geology* **39**, 499–502 (2011).

189. Edmonds, M. & Wallace, P. Volatiles and exsolved vapor in volcanic systems. *Elements* **13**, 29–34 (2017).
190. Wallace, P. J., Anderson, A. T. & Davis, A. M. Gradients in H_2O, CO_2, and exsolved gas in a large-volume silicic magma system: interpreting the record preserved in melt inclusions from the Bishop Tuff. *J. Geophys. Res. Sol. Earth* **104**, 20097–20122 (1999).
191. Walter, T. R. & Troll, V. R. Formation of caldera periphery faults: an experimental study. *Bull. Volcanol.* **63**, 191 (2001).
192. Seward, T. M., Williams-Jones, A. E. & Migdisov, A. A. in *Treatise of Geochemistry* Vol. 13 (eds. Holland, H. & Turekian, K.) 29–57 (Elsevier, 2014).
193. Dolejs, D. & Zajacz, Z. in *The Role of Halogens In Terrestrial and Extraterrestrial Geochemical Processes: Surface, Crust, and Mantle* (eds. Harlov, D. E. & Aranovich, L.) 431–543 (Springer, 2018).
194. Williams-Jones, A. & Migdisov, A. Experimental constraints on the transport and deposition of metals in ore-forming hydrothermal systems. *Soc. Econ. Geol. Spec. Publ.* **18**, 77–96 (2014).
195. Yao, Z., Mungall, J. E. & Jenkins, M. C. The Rustenburg Layered Suite formed as a stack of mush with transient magma chambers. *Nat. Commun.* **12**, 505 (2021).
196. Yao, Z. & Mungall, J. E. Magnetite layer formation in the Bushveld Complex of South Africa. *Nat. Commun.* **13**, 416 (2022).
197. Richards, J. P. et al. Contrasting tectonic settings and sulfur contents of magmas associated with cretaceous porphyry Cu±Mo±Au and intrusion-related iron oxide Cu-Au deposits in Northern Chile. *Econ. Geol.* **112**, 295–318 (2017).
198. Park, J. W., Campbell, I. H., Chiaradia, M., Hao, H. & Lee, C.-T. Crustal magmatic controls on the formation of porphyry copper deposits. *Nat. Rev. Earth Environ.* **2**, 542–557 (2021).
199. Bauer, T. E., Andersson, J. B. H., Sarlus, Z., Lund, C. & Kearney, T. Structural controls on the setting, shape, and hydrothermal alter- ation of the Malmberget iron oxide-apatite deposit, Northern Sweden. *Econ. Geol.* **113**, 377–395 (2018).
200. Andersson, J. B. H., Bauer, T. E. & Lynch, E. P. Evolution of structures and hydrothermal alteration in a Palaeoproterozoic supracrustal belt: constraining paired deformation-fluid flow events in an Fe and Cu-Au prospective terrain in northern Sweden. *Solid. Earth* **11**, 547–578 (2020).
201. Ridolfi, F. & Renzulli, A. Calcic amphiboles in calc-alkaline and alkaline magmas: thermobarometric and chemometric empirical equations valid up to 1,130 °C and 2.2 GPa. *Contrib. Miner. Petrol.* **163**, 877–895 (2012).
202. Mutch, E. J. F., Blundy, J. D., Tattitch, B. C., Cooper, F. J. & Brooker, R. A. An experimental study of amphibole stability in low-pressure granitic magmas and a revised Al-in-hornblende geobarometer. *Contrib. Mineral. Petrol.* **171**, 85 (2016).
203. Chelle-Michou, C., Rottier, B., Caricchi, L. & Simpson, G. Tempo of magma degassing and the genesis of porphyry copper deposits. *Sci. Rep.* **7**, 40566 (2017).
204. Chiaradia, M. & Caricchi, L. Supergiant porphyry copper deposits are failed large eruptions. *Commun. Earth Environ.* **3**, 107 (2022).
205. Audétat, A. The metal content of magmatic-hydrothermal fluids and its relationship to mineralization potential. *Econ. Geol.* **114**, 1033–1056 (2019).
206. Ortelli, M., Kouzmanov, K., Wälle, M. & Casanova, V. Fluid inclusion studies in opaque ore minerals: I. Trace element content and physical properties of ore minerals controlling textural features in transmitted near-infrared light microscopy. *Econ. Geol.* **113**, 1845–1860 (2018).
207. Casanova, V. et al. Fluid inclusion studies in opaque ore minerals: II. A comparative study of syngenetic synthetic fluid inclusions hosted in quartz and opaque minerals. *Econ. Geol.* **113**, 1861–1883 (2018).
208. Storey, C. R. & Smith, M. P. Metal source and tectonic setting of iron oxide-copper-gold (IOCG) deposits: evidence from an in situ Nd isotope study of titanite from Norrbotten, Sweden. *Ore Geol. Rev.* **81**, 1287–1302 (2017).
209. del Real, I., Thompson, J. F. H. & Carriedo, J. Lithological and structural controls on the genesis of the Candelaria-Punta del Cobre iron oxide copper gold district, Northern Chile. *Ore Geol. Rev.* **102**, 106–153 (2018).
210. Hu, H. et al. A genetic link between iron oxide-apatite and iron skarn mineralization in the Jinniu volcanic basin, Daye district, eastern China: evidence from magnetite geochemistry and multi-mineral U-Pb geochronology. *GSA Bull.* **132**, 899–917 (2019).
211. Ehrig, K. et al. Staged formation of the supergiant Olympic Dam uranium deposit, Australia. *Geology* **49**, 1312–1316 (2021).

Acknowledgements
Funding to M.R., F.B. and G.P. was provided by Millennium Science Initiative through Millennium Nucleus for Metal Tracing along Subduction Grant NC130065. Additional support was provided by FONDAP project 15090013 "Centro de Excelencia en Geotermia de Los Andes, CEGA", and FONDECYT grant #1190105.

Author contributions
All of the authors contributed to the discussion of the content as a team. M.R. wrote the paper with contributions from A.C.S., F.B., T.H., G.P. and L.D.B. Compilation of the data sets and preparation of figures was carried out by G.P., M.R. and T.H.

Competing interests
The authors declare no competing interests.

Peer review information
Nature Reviews Earth & Environment thanks V. Troll, B. Charlier and the other, anonymous, reviewer(s) for their contribution to the peer review of this work.

Publisher's note
Springer Nature remains neutral with regard to jurisdictional claims in published maps and institutional affiliations.

Supplementary information
The online version contains supplementary material available at https://doi.org/10.1038/s43017-022-00335-3.